This article has been accepted for publication in a future issue of this journal, but has not been fully edited. Content may change prior to final publication. Citation information: DOI 10.1109/ACCESS.2019.2921522, IEEE Access

Wireless Communications and Applications Above 100 GHz: Opportunities and Challenges for 6G and Beyond

Theodore S. Rappaport, Yunchou Xing, Ojas Kanhere, Shihao Ju,
Arjuna Madanayake, Soumyajit Mandal, Ahmed Alkhateeb, Georgios C. Trichopoulos
(Invited Paper)

***Abstract*—Frequencies from 100 GHz to 3 THz are promising bands for the next generation of wireless communication systems because of the wide swaths of unused and unexplored spectrum. These frequencies also offer the potential for revolutionary applications that will be made possible by new thinking, and advances in devices, circuits, software, signal processing, applications, and systems. This paper describes many of the technical challenges and opportunities for wireless communication and sensing applications above 100 GHz, and presents a number of promising discoveries, novel approaches, and recent results that will aid in the development and implementation of the sixth generation (6G) of wireless networks, and beyond. This work shows recent regulatory and standard body rulings that are anticipating wireless products and services above 100 GHz, and illustrates the viability of wireless cognition, hyper-accurate position location, sensing and imaging. This paper also presents approaches and results that reduce the computational complexity and simplify the signal processing used in adaptive antenna arrays, by exploiting the Special Theory of Relativity to create a "cone of silence" in over-sampled antenna arrays that improves performance for digital phased array antennas. Also, new results that give insights into power efficient beam steering algorithms, and new propagation and partition loss models above 100 GHz are given, and promising imaging, array processing, and position location results are presented. The implementation of spatial consistency at THz frequencies, an important component of channel modeling that considers minute changes and correlations over space, is also discussed. This paper offers the first in-depth look at the vast applications of THz wireless products and applications, and provides approaches for how to reduce power and increase performance across several problem domains, giving early evidence that THz techniques are compelling and available for future wireless communications.**

***Index Terms*—mmWave; 5G; D-band; 6G; channel sounder; propagation measurements; Terahertz (THz); array processing; imaging; scattering theory; cone of silence; digital phased arrays; digital beamformer; signal processing for THz; position location; channel modeling; THz applications; wireless cognition; network offloading**

I. Introduction

The tremendous funding and research efforts invested in millimeter wave (mmWave) wireless communications, and the early success of 5G trials and testbeds across the world, ensure that commercial wide-spread 5G wireless networks will be realized by 2020 [1]. The use of mmWave in 5G wireless communication will solve the spectrum shortage in current 4G cellular communication systems that operate at frequencies below 6 GHz [2]. However, the increasing number of new applications such as virtual/augmented reality (VR/AR), autonomous driving, Internet of Things (IoT), and wireless backhaul (as a replacement for labor-intensive installation of optical fiber) [3], [4], as well as newer applications that have not been conceived yet, will need even greater data rates and less latency than what 5G networks will offer.

Today, within the global unlicensed wireless mmWave band of 60 GHz, there is $\sim$ 7 GHz of bandwidth available [5], and in such a wide bandwidth, data rates on the order of 100 Gigabits per second (Gbps) can only be achieved with transmission schemes having a spectral efficiency of at least 14 bit/s/Hz, which requires symbol fidelity that is not feasible using currently known digital modulation techniques or transceiver components [6]–[8]. Therefore, data rates on the order of 100 Gbps or more will flourish at frequencies above 100 GHz, where the available spectrum is massively abundant [9].

Fig. 1 illustrates the applications and range of frequencies available from the sub-THz regime up through and beyond the optical spectrum, and shows how mmWaves and THz frequencies are three and two orders of magnitude, respectively, below the frequencies of visible light. At optical and infrared frequencies, issues like the impact of atmospheric and water absorption on the signal propagation, ambient sunlight, required low transmission power budget due to eye-safety limits, and high diffusion losses on rough surfaces limit their use for wireless communication systems [10]. Ionizing radiation, which includes ultraviolet, x-rays, galactic radiation, and gamma-rays, is dangerous since it is known to have sufficiently high particle energy to dislodge electrons and create free-radicals that can lead to cancer [11], [12] and is believed to be a major health risk for interplanetary travel [12], [13]. The adverse health effects of ionizing radiation may be negligible, however, if used with care [14]. Ionizing radiation can be used for gauging the thickness of metals, Roentgen Stereophotogrammetry, astronomy, nuclear medicine, sterilizing medical equipment, and pasteurizing certain foods and spices [15]. Unlike ionizing radiation, mmWave and THz radiation is nonionizing because the photon energy is not nearly sufficient (0.1 to 12.4 meV, which is more than three orders of magnitude weaker than ionizing photon energy levels) to release an electron from an atom or a molecule, where typically 12 eV is required for ionization [11], [12], [16]. Since ionizing radiation is not known to be a concern at mmWave and THz frequencies, and

This article has been accepted for publication in a future issue of this journal, but has not been fully edited. Content may change prior to final publication. Citation information: DOI 10.1109/ACCESS.2019.2921522, IEEE Access

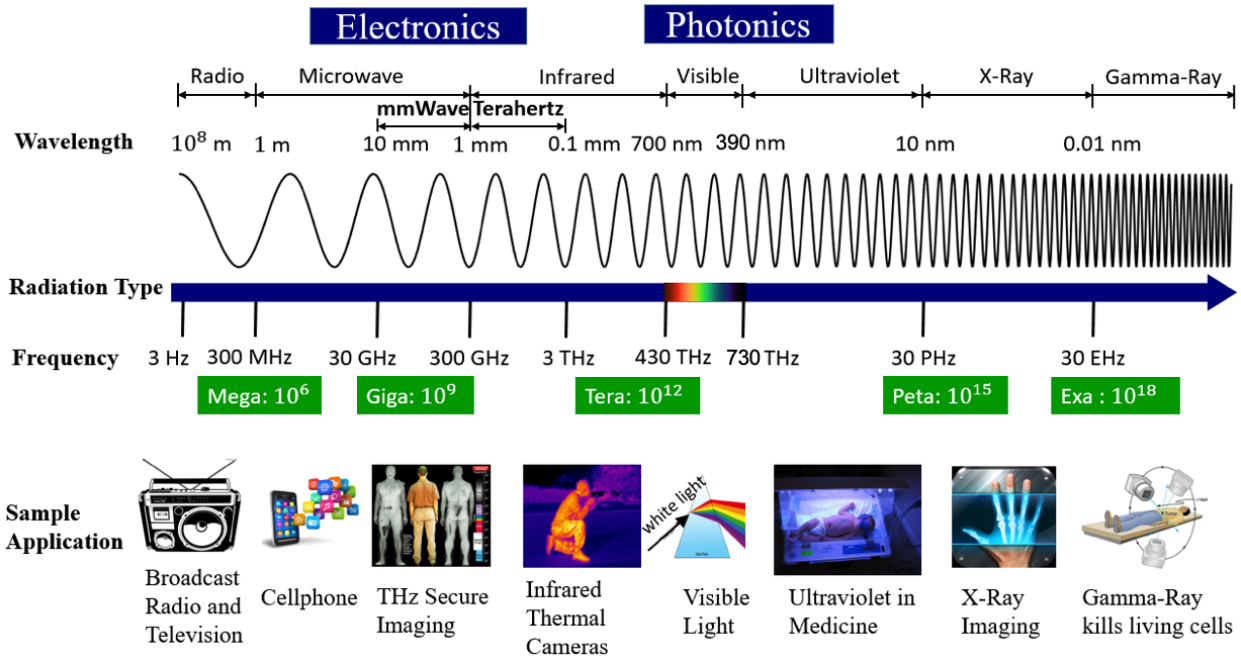

Fig. 1: The electromagnetic spectrum, and various applications as a function of frequency.

heating is believed to be the only primary cancer risk [11], the Federal Communications Commission (FCC) and International Commission on Non-Ionizing Radiation Protection (ICNIRP) standards [17], [18] are designed principally to protect against thermal hazards, particularly for the eyes and skin where these tissues are most sensitive to heat from radiation due to lack of blood flow. However, we must point out that with the likelihood of THz sources becoming more widely available, there should be careful work done to understand the biological and molecular impact of THz radiation on human health [12], since, even though THz is three orders of magnitude lower in frequency than ionizing radiation, it would be prudent to know with certainty that heating is the only health concern at THz [11].

While 5G, IEEE 802.11ay, and 802.15.3d [19], [20] are being built out for the mmWave spectrum and promise data rates up to 100 Gbps, future 6G networks and wireless applications are probably a decade away from implementation, and are sure to benefit from operation in the 100 GHz to 1 THz frequency bands where even greater data rates will be possible [3], [7], [10]. The short wavelengths at mmWave and THz will allow massive spatial multiplexing in hub and backhaul communications, as well as incredibly accurate sensing, imaging, spectroscopy, and other applications described subsequently in this paper [21]–[24]. The THz band, which we shall describe as being from 100 GHz through 3 THz, can also enable secure communications over highly sensitive links, such as in the military due to the fact that extremely small wavelengths (orders of microns) enable extremely high gain antennas to be made in extremely small physical dimensions [25].

There are tremendous challenges ahead for creating commercial transceivers at THz frequencies, but global research is addressing the challenges. For example, the DARPA T-MUSIC program is investigating SiGe HBT, CMOS/SOI and BiCMOS circuit integration, in hopes of achieving power amplifier threshold frequencies f_t of 500-750 GHz [26]. A survey of power amplifier capabilities since the year 2000 is given by [27]. It should be clear that the semiconductor industry will solve these challenges, although new architectures for highly dense antenna arrays will be needed, due to the small wavelengths and physical size of RF transistors in relation to element spacing in THz arrays. Section III provides some promising design approaches for future digital arrays.

Since there is very high atmospheric attenuation at THz band frequencies, especially at frequencies above 800 GHz (see Fig. 6), highly directional "pencil" beam antennas (antenna arrays) will be used to compensate for the increased path loss due to the fact that the gain and directivity increase by the square of the frequency for a fixed physical antenna aperture size [6], [28]. This feature makes THz signals exceedingly difficult to intercept or eavesdrop [4], [10], [25], [29]. However, a narrow pencil-like beam does not guarantee immunity from eavesdropping, and physical-layer security in THz wireless networks and transceiver designs that incorporate new countermeasures for eavesdropping will be needed [30].

Energy efficiency is always important for communication systems, especially as circuitry moves up to above 100 GHz, and a theoretical framework to quantify energy consumption in the presence of vital device, system, and network trade-offs was presented in [31], [32]. The theory, called the *consumption factor theory* (CF, with a metric measured in bps/W), provides a means for enabling quantitative analysis and design approaches for understanding power trade-offs in any communication system. It was shown in [31], [32] that the efficiency of components of a transmitter closest to the output, such as the antenna, have the largest impact on CF [31]. The power efficiency increases with increasing bandwidth when most of the power used by components that are "off", e.g., ancillary, to the signal path (e.g., the baseband processor, oscillator, or

This article has been accepted for publication in a future issue of this journal, but has not been fully edited. Content may change prior to final publication. Citation information: DOI 10.1109/ACCESS.2019.2921522, IEEE Access

a display) is much greater than the power consumed by the components that are in line with the transmission signal path (e.g., power amplifier, mixer, antenna) [31], [32]. For a very simple radio transmitter, such as one that might be used in low cost IoT or "smart dust" applications where the power required by the ancillary baseband processor and oscillator is small compared to the delivered radiated power, the power efficiency is independent of the bandwidth [31]. Thus, contrary to conventional wisdom, the CF theory proves that for antennas with a fixed physical aperture, it is *more energy efficient* to move up to mmWave and THz frequencies which yield much wider bandwidth and better power efficiency on a bits per second per watt (bps/W) basis, as compared to the current, sub-6 GHz communication networks.

TABLE I: UNLICENSED SPECTRUM PROPOSED BY FCC [33]

Frequency Band (GHz)	Contiguous Bandwidth (GHz)
116-123	7
174.8-182	7.2
185-190	5
244-246	2
Total	21.2

Global regulatory bodies and standard agencies such as the FCC [33], the European Telecommunication Standards Institute (ETSI) [34], and the International Telecommunication Union (ITU) [35], are seeking comments to allocate frequency bands above 95 GHz for point-to-point use, broadcasting services, and other wireless transmission applications and use cases [36]–[39]. In fact, in March 2019, the FCC voted to open up spectrum above 95 GHz for the first time ever in the USA, and provided 21.2 GHz of spectrum for unlicensed use shown in Table I, and permitted experimental licensing up to 3 THz [40]. The mmWave coalition [41], which is a group of innovative companies and universities united in the objective of removing regulatory barriers to technologies using frequencies ranging from 95 GHz to 275 GHz in the USA, submitted comments to the FCC and to the National Telecommunications and Information Administration (NTIA) for developing a sustainable spectrum strategy for America's future, and urged NTIA to facilitate greater access to spectrum above 95 GHz for non-Federal use in January 2019 [41]. The Institute of Electrical and Electronics Engineers (IEEE) formed the IEEE 802.15.3d [20] task force in 2017 for global Wi-Fi use at frequencies from 252 GHz to 325 GHz, creating the first worldwide wireless communications standard for the 250-350 GHz frequency range, with a nominal PHY data rate of 100 Gbps and channel bandwidths from 2 GHz to 70 GHz [20]. The use cases for IEEE 802.15.3d include kiosk downloading (dubbed the "Information Shower" by an author of this paper) [42], intra-device radio communication [43], connectivity in data centers, and wireless fiber for fronthaul and backhaul [20], [41], [44].

This paper is organized as follow: Section II provides insights into mmWave and THz applications. Section III explores the possibility of using array signal processing techniques for improved front-end performance at frequencies above 100 GHz. Section IV demonstrates viability for true time delay (TTD) beamformers for wideband digital arrays. Section V reviews key wireless propagation fundamentals and presents measurements and research above 100 GHz which could be used for many novel applications, including future 6G communications. Channel sounding systems and measured results at above 100 GHz are given in Section VI, respectively. 28, 73 and 142 GHz channels are compared in Section VII. Scattering mechanism at mmWave and THz frequencies is explained in Section VIII. Section IX investigates positioning approaches (e.g., position location that can be used in navigation) at THz frequencies that promise unprecedented accuracy. Section X discusses the implementation of spatial consistency, an important component of channel modeling at THz frequencies, and Section XI concludes the paper and summarizes key areas that warrant future research.

TABLE II: PROMISING APPLICATIONS AT MMWAVE AND THZ

mmWave & THz Applications–the potential for 6G	
Application	**Example Use Cases**
Wireless Cognition	Robotic control [45], [46]
	Drone fleet control [45]
	Autonomous vehicles [47]
Sensing	Air quality detection [24]
	Personal health monitoring systems [48]
	Gesture detection [22]
	Explosive detection and gas sensing [49]
Imaging	See in the dark (mmWave Camera) [50]
	High-definition video resolution radar [21]
	THz security body scan [23]
Communication	Mobile wireless communications [51], [52]
	Wireless fiber for backhaul [4]
	Intra-device radio communication [43]
	Connectivity in data centers [10]
	Information shower ($\geq$100 Gbps) [42]
Positioning	Centimeter-level positioning [50], [53]

II. MMWAVE AND THZ APPLICATIONS

The ultra-high data rates facilitated by mmWave and THz wireless local area and cellular networks will enable super-fast download speeds for computer communication, autonomous vehicles, robotic controls, the information shower [42], high-definition holographic gaming, entertainment, video conferencing, and high-speed wireless data distribution in data centers [10]. In addition to the extremely high data rates, there are promising applications for future mmWave and THz systems that are likely to evolve in 6G networks, and beyond. These applications can be categorized into main areas such as wireless cognition, sensing, imaging, wireless communication, and position location/THz navigation (also called localization, or positioning), as summarized in Table II.

A. Wireless cognition

Wireless cognition is the concept of providing a communication link that enables massive computations to be conducted

This article has been accepted for publication in a future issue of this journal, but has not been fully edited. Content may change prior to final publication. Citation information: DOI 10.1109/ACCESS.2019.2921522, IEEE Access

remotely from the device or machine that is doing real time action [46]. For example, a lightweight drone fleet may not have the power or weight budget to conduct massive computations on board the apparatus, but with a wide enough channel bandwidth and sufficiently fast data rate, real time computations for extremely complex tasks, such as contextual awareness, vision, and perception may be carried out at a fixed base station or edge server that is in wireless connection and supporting real time cognition for the drone fleet. Robots, autonomous vehicles, and other machines may be similarly designed to exploit cognitive processing performed remotely from the machine using wireless, with the ability to perform tasks without the benefit of local cognition on the platform [45], [46].

When one considers the growth of computational power provided by Moore's law, it can be seen that the modest price of 1000 USD (the cost of today's smart phone) will likely be able to purchase a computer with computational capabilities that are on the order of the human brain by the year 2036. This observation stems from results in [54], [55] which extrapolate the increase in computational capabilities over time since 1965 [56]. The following analysis shows that Terahertz frequencies will likely be the first wireless spectrum that can provide the real time computations needed for wireless remoting of human cognition [52].

There are about 100 billion (10^{11}) neurons in the human brain, each of which can fire 200 times per second (5 ms update rate), and each neuron is connected to about 1000 others, resulting in a computation speed of 20×10^{15} floating-point operations per second (flops) [54], [55], which, if each operation is assumed to be binary, will require a data rate of 20,000 Tbps:

$$\begin{aligned} &\text{Human Brain flops (Computation Speed)} \\ &= 10^{11} \text{ neurons} \times 200 \text{ flop/sec} \times 10^{3}/\text{neuron} \\ &= 20 \times 10^{15} \text{ flop/sec} = 20 \text{ petaflops/sec} \times 1 \text{ bit/flop} \\ &= 20,000 \text{ Tbps}. \end{aligned} \tag{1}$$

Each neuron has write access to 1000 bytes resulting in a memory size of the human brain of 100 Terabytes [54], [55]:

$$\begin{aligned} \text{Storage} &= 10^{11} \text{ neurons} \times 10^{3} \text{ bytes/neuron} \\ &= 10^{14} \text{ bytes} = 100 \text{ TB}. \end{aligned} \tag{2}$$

Today's state-of-the art 1000 USD computer technology performs one trillion (e.g., 10^{12}) computations/sec, which is four orders of magnitude less than the speed of the human brain. Future wireless generations (e.g., 6G or 7G) are likely to allocate up to 10 GHz RF channels for each user in the THz regime, and by assuming that each user is able to exploit 10 bits/symbol modulation methods and 1000 times increase in channel capacity using yet-to-be-invented concepts beyond cooperative multipoint (CoMP) and Massive-MIMO, it is readily seen in (3) that data rates of 100 Terabytes/sec will be achieved.

$$\begin{aligned} R &= 10 \text{ GHz channel} \times 10 \text{ bits/(sec} \cdot \text{Hz)} \times 10^{3} \\ &= 100 \text{ Tbps}. \end{aligned} \tag{3}$$

From (1) and (2), it is clear that a 100 Tbps link is plausible in a 10 GHz channel bandwidth, providing 0.5% of real time human computational power. Ambitiously, if 100 GHz channel bandwidths are used, 1 Petabits/sec of information, or 5% of the real time computational power of the human brain, could be carried over wireless [52].

B. Sensing

Sensing applications enabled by mmWave and THz frequencies exploit the sub-mm wavelength and frequency selectivity of the measured environment to gain knowledge about the environment based on the observed signature of the propagated signal. Sensing applications may exploit both the vastly wider channel bandwidths at above 100 GHz, as well as the frequency-selective resonances and absorption of various materials. The ability to implement very high gain antennas in a small physical form factor also enables sensing applications that are very directional, and as frequencies increase, the spatial resolution becomes much finer as a function of wavelength, thereby enabling sub-millimeter spatial differentiation as frequencies exceed 300 GHz.

Through beam scanning, it will become possible to create images of physical spaces, through the systematic monitoring of received signal signatures at a wide array of different angles. Because electrical beam steering algorithms can be implemented in real time (sub microsecond) and radio propagation distances are small (e.g., on the order of meters in a room) thus lending to propagation times that are less than 10 ns, it shall be feasible to measure the properties of a room, an office, or a complex environment in a matter of seconds or less. This ability opens up a new dimension of wireless, that enables future wireless devices to do "wireless reality sensing" and gather a map or view of any location, leading to detailed 3-D maps of the world created on the fly and uploaded/shared on the cloud by future devices [57], [58]. Also, since certain materials and gasses have vibrational absorption (e.g., resonances) at particular frequencies throughout the THz band, it becomes possible to detect the presence of certain items based on frequency scanning spectroscopy.

THz will enable new sensing applications such as miniaturized radars for gesture detection and touchless smartphones, spectrometers for explosive detection and gas sensing [49], THz security body scanning, air quality detection [24], personal health monitoring systems [48], precision time/frequency transfer, and wireless synchronization [10], [22], [59]. By building real time maps of any environment, it may also be possible to predict channel characteristics at a mobile device, to aid in the alignment of directional antennas, to provide on-the-fly position location, as well as adaptation of wireless capabilities [53]. This capability could also be fed to the cloud to enable a real time collection capability for mapping and sensing the world, which then could be used in commercial applications for transportation, shopping, and other retail uses.

C. Imaging

Radar at mmWave and THz frequencies are more effective than light or infrared-based imaging such as Light Detection and Ranging (LIDAR), due to the smaller impact that weather and ambient light have on the THz channel. It is worth noting

This article has been accepted for publication in a future issue of this journal, but has not been fully edited. Content may change prior to final publication. Citation information: DOI 10.1109/ACCESS.2019.2921522, IEEE Access

that although LIDAR can provide higher resolution, LIDAR cannot work when it is foggy, raining, or cloudy [60]. However, mmWave and THz radar can be used for assisting driving or flying in foul weather, as well as in military and national security [10], [21], [25]. High-definition video resolution radars that operate at several hundred gigahertz will be sufficient to provide a TV-like picture quality and will complement radars at lower frequencies (below 12.5 GHz) that provide longer range detection but with poor resolution [21], [23]. Dual-frequency radar systems will enable driving or flying in very heavy fog or rain [21].

THz waves can augment human and computer vision to see around corners and to "view" NLOS objects, which enables unique capabilities in rescue and surveillance, autonomous navigation, and localization. A building surface (e.g., wall, floor, door) typically behaves to a first order as mirrors (e.g., perfect reflectors of THz energy), thus allowing THz imaging to see around corners and behind walls if there are sufficient reflection or scattering paths (see Section VIII) [61], [62]. NLOS imaging methods based on visible and infrared light have also been proposed in [63]–[65]. However, the optical wavelength is smaller than the surface roughness of most surfaces, thus optical NLOS imaging requires complex hardware and computationally expensive reconstruction algorithms, while exhibiting short imaging distances ($<$ 5 m). In general, the practical deployment of visible light systems is still not clearly evolved due to weakly scattered signals, small field of view, and long integration times.

Alternatively, lower frequency ($<$ 10 GHz) NLOS radar systems suffer less loss and objects appear relatively much smoother. However, in the lower frequency spectrum, materials are semitransparent, edge diffraction become much stronger, and images are easily cluttered due to strong multi-reflection propagation [66]–[70]. Additionally, radar systems require accurate knowledge of the static geometry and are limited to object detection rather that detailed images of the hidden scene.

THz waves combine many of the advantageous traits of both microwaves and visible light. Namely, they feature small wavelengths and wide bandwidths that allow high spatial resolution images with moderately sized imaging systems [71], [72]. Additionally, THz scattering exhibits both specular and diffuse scattering from most building surfaces, as depicted in Fig. 2 (see Section VIII for further details). The strong specular component turns the surfaces into something close to "electrical mirrors", thus allowing to image objects around obstacles, while maintaining spatial coherency (narrow beams) and high spatial resolution [62]. Radar imaging systems illuminate the scene with THz waves and generate 3D images by computing the time of flight (ToF) of the backscattered signals. When the path of the scattered signal involves multiple bounces on surrounding surfaces, the resulting 3D image appears distorted. If the LOS surfaces act as mirrors due to the strong specular reflections, a corrected image of the NLOS objects can be reconstructed by applying relatively simple mirroring transformations [61].

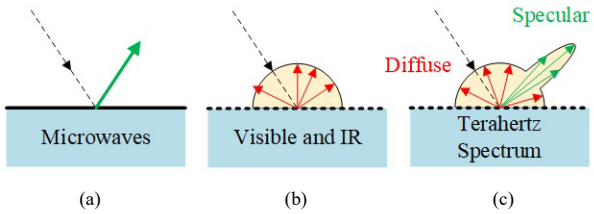

Fig. 2: Surface scattering across the EM spectrum a) Most surfaces appear smooth at microwave frequencies (specular scattering), b) Same surfaces exhibit significant considerable roughness in optical spectrum (diffuse scattering) c) in THz regime most building surfaces exhibit significant diffuse scattering and strong specular reflections.

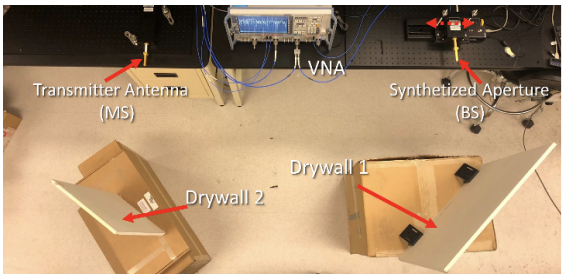

(a) Experimental Setup

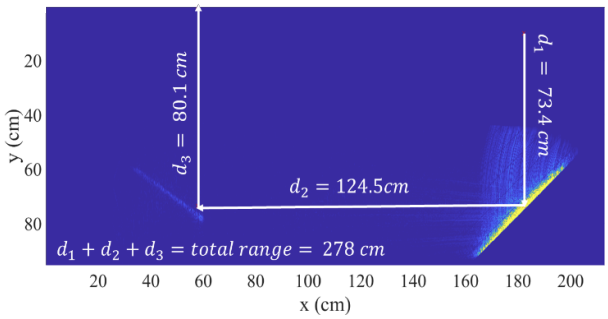

(b) Use Projection on the mmWave Image

Fig. 3: Leveraging mmWave imaging and communications can position devices with centimeter accuracy, even in NLOS scenarios. Figure (a) shows the experimental setup adopted by [50] to illustrate the capability of mmWave imaging-based positioning. In Figure (b) the user location is projected on the constructed mmWave image.

D. Precise Positioning

Leveraging mmWave imaging and communications for centimeter-level localization is an exciting feature that will likely be incorporated in future portable devices operating above 100 GHz [52]. A simple example of what is possible was illustrated in [50] using an experimental setup, as shown in Fig. 3(a). The experiment demonstrates excellent accuracy when a LOS does not exist, and illustrates how positioning and sensing will become part of communication devices. Figure 3(a) shows the setup, which consists of (i) a synthetic aperture radar (SAR) emulating a 13-cm aperture linear antenna array and operating at 220-300 GHz, (ii) two drywall sheets, and (iii) a single-antenna user that is in the NLOS of the SAR. First, a mmWave image (e.g., map) of the surrounding environment, including both LOS and NLOS objects, is constructed by rapid beam steering and analyzing the radar returns at very narrow beam angle separations. Second, the user sends an uplink pilot that is used by the antenna array, for example at a base station

This article has been accepted for publication in a future issue of this journal, but has not been fully edited. Content may change prior to final publication. Citation information: DOI 10.1109/ACCESS.2019.2921522, IEEE Access

or an access point, to estimate the angle and time of arrival (AOA and TOA). Finally, the AOA and TOA are used to back-track the path of the user signal on the constructed mmWave image, as shown in Fig. 3(b), to determine the user location (see Section II-D for more details). Considering Fig. 3(a), this mmWave imaging/communication-based method was able to localize the user within a 2 cm radius over a distance of 2.8 m, and as shown in Section IX, excellent accuracy are possible over much greater distances.

Leveraging mmWave and THz imaging for localization has interesting and unique benefits compared to other methods. The mmWave imaging/communication methods proposed in [50], [53], [58] can localize users in the NLOS areas, even if their travel paths to the base station/access points experience more than one reflection (e.g., multiple bounces). For example, the experiment in Fig. 3(a) was able to localize the user even though its path experiences two bounces. Further, different from classical simultaneous localization and mapping (SLAM) methods, which require prior knowledge and calibration of the environment, the proposed mmWave imaging/communication-based technique in [50] does not require any prior knowledge of the environment. By building or downloading the map of the environment, the mobile device will be able to exploit many other capabilities, such as predicting the signal level, using real time site-specific prediction [57], or uploading the map to the cloud that compiles physical maps, or which uses such maps for mobile applications [50], [53], [58]. Finally, due to leveraging the large bandwidth available at frequencies above 100 GHz, the LOS and NLOS users can be localized with centimeter accuracy. These promising user features highlight the potential of merging mmWave imaging and communications for precise positioning in 6G systems and beyond.

Using mmWave or THz imaging (e.g., a mmWave camera as discussed in Section II-C) to reconstruct 3D maps of the surroundings in unknown environments, it will be possible to merge sensing and imaging and position location all at the same time. As shown subsequently, mmWave and THz signals reflect strongly from most building materials which enable imaging of hidden objects (NLOS imaging) [50], [53], [58], although as shown in Section VIII, scattering can also be well modeled and predicted. Based on the 3D maps of the physical surroundings, and the time and angular information from a mobile (TOA and AOA), centimeter level localization and mapping are achievable with the massive bandwidth and large antenna arrays at mmWave and THz frequencies [50], [53], [58].

III. Multi-Port Array Transceiver Architectures Based on Space-Time Sigma-Delta Theory

The adoption of mmWave and THz frequency bands above 100 GHz may require new approaches to transceiver front-end design, due to the challenges of power efficiency and the vastly increased number of antennas that will be possible in a small physical area. In fact, the physical size of RF amplifiers may not be small enough to be physically located behind individual antenna elements at THz frequencies, possibly necessitating hybrid beamforming approaches for practical implementations [73], [74].

Key transceiver performance metrics such as i) noise figure (NF) and linearity of the low-noise amplifier (LNA), and ii) the peak output power P_{sat} and power-added efficiency (PAE) of the power amplifier, degrade rapidly with increasing operating frequency f_0 [6], [27], [75]. For example, a survey of the recent literature shows the product of P_{sat}, gain, and PAE scales as $1/f_0^2$ [27]. Phase noise also increases with frequency, creating increased noise levels for practical coherent demodulation. Thus, it becomes challenging to provide sufficient performance at these frequencies to facilitate higher-order modulations, such as those adopted by modern 5G wireless and Wi-Fi systems. The larger number of antennas used at mmWave and THz frequencies begs consideration of array signal processing techniques that can lead to improved antenna array performance in the face of noise and linearity limitations for mmWave and THz transceivers. In this section, we illustrate a promising new technique of spatially-oversampled antennas, and present new phased array device architectures and compact computational approaches that can provide accurate beam steering with exponentially less power and physical chip real estate than today's methods of phased array beamforming.

A mmWave digital phased array transmits and receives far-field propagating electromagnetic plane-waves. One promising viewpoint is to consider the spatio-temporal frequency-domain region of support (ROS) of these plane-waves as a region of causality that contains all possible signals of interest seen by the array, while ignoring all other components outside of the ROS [76]–[80]. This region of causality, which is a frequency-domain version of the light-cone that is well-described by the Special Theory of Relativity, is a conical region of the spatio-temporal frequency domain inside of which all plane-waves for a given space-time beam pattern are constrained to exist (see Fig. 4). For a Nyquist-sampled planar antenna array in the x-y plane, the cone-shaped frequency domain region defined by the surface $\omega_x^2 + \omega_y^2 = \omega_{ct}^2$ contains all propagating RF beams used for wireless communications, where ω_x and ω_y are spatial frequencies for the wave along the x and y axes, while ω_{ct} is its temporal frequency in units such that the speed of light is unity. When the antenna arrays are spatially-oversampled (see Fig. 4(a)), the cone-shaped ROS becomes correspondingly narrower, with a surface given by $\omega_x^2 + \omega_y^2 = \omega_{ct}^2/K_u^2$ where $K_u \in \mathbb{Z}^+$ is the spatial over-sampling factor (see Fig. 4(b)). Specifically, the opening angle of the cone is given by $\theta' = \tan^{-1}(1/K_u)$ (see Fig. 4(b)), which decreases as K_u increases. Thus, the fractional volume of 3-D spacetime occupied by the cone-shaped ROS of all propagating waves decreases with K_u.

In other words, spatial oversampling of the antenna array makes the cone *increasingly sparse* within 3-D spacetime. As a simple numerical example, consider a carrier frequency of 300 GHz, corresponding to a free-space wavelength of $\lambda = 1$ mm. A conventional Nyquist-sampled antenna array would have an antenna spacing of $\lambda/2 = 0.5$ mm, resulting in an open cone angle $\theta' = 45°$. By contrast, a $4\times$ spatially-oversampled array would have an oversampled antenna spacing of $\lambda/8 = 0.125$ mm, resulting in $\theta' = 14.0°$. Such sparsity does not allow the array to generate sharper beams (since beam width is ultimately limited by the total aperture), but does result in other benefits in terms of reduced noise figure

This article has been accepted for publication in a future issue of this journal, but has not been fully edited. Content may change prior to final publication. Citation information: DOI 10.1109/ACCESS.2019.2921522, IEEE Access

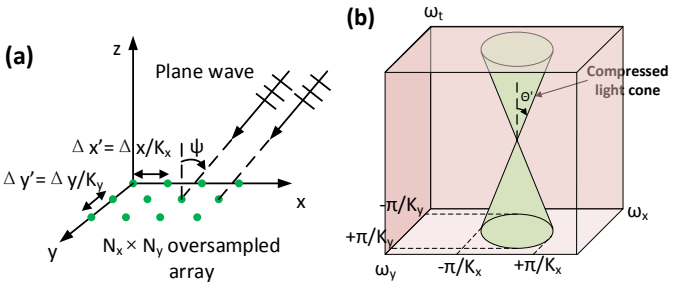

Fig. 4: (a) A spatially-oversampled $N_x \times N_y$ uniform rectangular antenna array (URA). The antenna spacing is $\lambda_m/(2K_x)$ and $\lambda_m/(2K_y)$ along the x-and y-axes, respectively. Here λ_m is the electromagnetic wavelength, $K_x \geq 1$ and $K_y \geq 1$ are the spatial oversampling factors along x and y, respectively, and assume $K_x = K_y = K_u$ for convenience. (b) The ROS of waves received by the 2-D URA (green) consists of a narrow light cone that is sparse in the 3-D spacetime frequency domain.

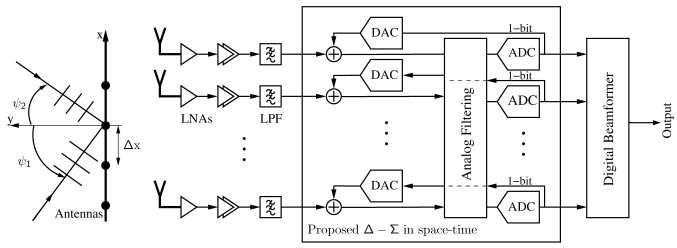

Fig. 5: An overview of a space-time $\Delta - \Sigma$ ADC where spatio-temporal noise-shaping occurs along both spatial- and temporal-frequency domains. The analog filtering module inside the multi-port ADC couples the inputs and output ports in such a manner that the quantization noise arising from the 1-bit quantizers are shaped to be outside the K_u-compressed "cone of silence" of the array. The plane-wave signals of interest, on the other hand, now lie inside the "cone of silence" and can be extracted by a sharp digital beamformer whose minor lobes will significantly attenuate the quantization noise of the system.

(NF), increased linearity, and a relaxing of the requirement of analog-to-digital converters or digital-to-analog converters (ADCs/DACs) resolution, as described in more detail in the next sub-section.

A. Cones of Silence in Antenna Arrays

For a given spatial over-sampling factor K_u, all possible electromagnetic plane-waves and their beam-shaped wideband spectral ROSs across an antenna array lie inside the cone-shaped region of causality. Because of relativistic constraints, no propagating waves can exist outside this region. This is a direct result of the nature of the wave equation as observed in the frequency domain. Thus, the rest of the spectral domain is devoid of any propagating waves. Hence we denote the cone-shaped ROS defined by a particular antenna array's over-sampling factor as an array's "cone of silence", and our design mission becomes one of shifting all possible noise and distortion to outside of this cone. Such cones directly arise from fundamental physics, namely the causality of electromagnetic plane-waves in the spacetime frequency domain $(\omega_x, \omega_y, \omega_{ct}) \in \mathbb{R}^3$ [76]–[80], and are thus present for all uniformly-spaced rectangular arrays. We now show that these naturally occurring "cones of silence" can be quite effective in improving the performance of antenna array electronics as the industry moves to THz bands.

B. Moving from N 2-port Tansceivers to one Multi-Port Transceiver for Array Processing

In conventional digital phased array transceivers, a single transceiver is replicated *N* times to form an *N*-element array. In the proposed approach, these *N* individual transceivers are replaced by a single multi-port transceiver. For example, *N* conventional multi-bit ADCs in an *N* element array are replaced by a single K_uN-port ADC which uses 1-bit resolution. The multi-port ADC takes in K_uN number of analog inputs and produces K_uN number of 1-bit digital outputs. The algorithm, implemented in circuit form, shapes noise and distortion in both space- and time-frequency domains, such that the dominant parts of noise and distortion energy lies outside the "cone of silence" of the signals of interest. The fact that the noise and distortion has been shaped to be outside the "cone of silence", while the signal of interest itself lies inside it, allows lower-resolution ADC outputs to be employed in an K_uN element digital beamformer that generates outputs with *a higher digital resolution than in conventional N-element array receivers*. Such multi-port flash ADCs have the potential to achieve $\approx 2^{K_u}$(i.e., exponential) savings in number of comparators at a K_u (i.e. linear) cost in number of antennas. The idea of noise shaping is motivated by the fact that, at sub-THz carrier frequencies with basebands spanning tens of GHz, fully-digital arrays having K_uN number of "crude 1-bit ADCs making up the multi-port ADC" is possible, unlike building *N* high-resolution ADCs for conventional arrays, which is more extensive from a power and part count perspective. The noise-shaping approach allows a spatially over-sampled dense 1-bit receiver array to have the same quantization noise performance as a 3-4 bit resolution array which is Nyquist spaced.

C. Spatially Noise-Shaped Circuits for Antenna Arrays

The fact that "cones of silence" exist for all phased arrays and become increasingly sparse in 3-D spacetime as K_u increases was previously exploited to improve array performance, but offers even greater promise for mmWave and Terahertz phased array antennas. As was first shown in [81] and later expanded upon in [82]–[86], it is possible to exploit such multi-dimensional spatio-temporal feedback between the individual transceiver channels, i.e., along both spatial as well as temporal dimensions. These feedback loops emulate the performance of $\Delta - \Sigma$ algorithms, which are widely used to improve the resolution of ADCs and digital-to-analog converters (DACs) [6], [87]. Fig. 5 shows an example $\Delta - \Sigma$ ADC and LNA compared with the topology of a conventional digital phased array. A critical and valuable practical result of using the phased array architecture in Fig. 5 is that it becomes possible to use RF circuitry (which may be physically large compared to antenna element spacing) behind numerous antenna elements (either in a true digital or hybrid beamforming implementation). Conventional array designs simply may not be able to accommodate, physically, the RF transistors in a phased array package.

A conventional $\Delta - \Sigma$ ADC is designed to separate desired signals (i.e., the inputs to be digitized) from undesired ones (i.e., quantization noise) along the temporal frequency

This article has been accepted for publication in a future issue of this journal, but has not been fully edited. Content may change prior to final publication. Citation information: DOI 10.1109/ACCESS.2019.2921522, IEEE Access

axis, thus increasing the ADC's precision beyond that of its quantizer. In fact, many $\Delta - \Sigma$ ADCs use a 1-bit quantizer (i.e., a single comparator) but nevertheless provide several bits of effective resolution (i.e., effective number of bits or ENOB$\gg 1$). Such improved performance arises by combining two key principles: i) *temporal oversampling* to expand the frequency range over which the ADC's quantization noise is spread, thus reducing its power spectrum density (PSD); and ii) *noise shaping* to actively filter quantization noise out of the small frequency range (at low frequencies) within which the input signals of interest must be confined (due to oversampling). Note that a $\Delta - \Sigma$ DAC operates in a fundamentally similar way, but with the roles of the analog input and digital output signals reversed.

The key point exploited in [81]–[86] is that the potential benefits of i) spatially oversampling an antenna array, and ii) shaping unwanted thermal and quantization noise of the array electronics away from the "cone of silence" occupied by propagating electromagnetic waves, are *exactly analogous to those provided by temporal oversampling and noise shaping in a conventional $\Delta-\Sigma$ ADC or DAC*. In particular, it becomes clear that it is possible to add appropriate spatial-domain, and spatio-temporal domain feedback loops (i.e., carefully-designed electrical coupling networks between the amplifiers and data converters present in adjacent transceiver channels as shown in Fig. 5) that mimic the noise shaping provided by a $\Delta - \Sigma$ converter, *but in the spatio-temporal (rather than temporal) frequency domain*. As a result, the thermal noise, quantization noise, and nonlinear distortion added by low-noise amplifiers (LNAs), ADCs, and DACs within the array can be actively shaped to lie outside the array's "cone of silence", effectively separating them from the propagating electromagnetic waves received or transmitted by the antennas. As a result, spatial noise shaping improves all the important performance metrics for a receive array: it reduces NF, greatly increases linearity, and significantly increases ENOB [85], [86]. These improvements enable receiver power consumption to be reduced for a given set of performance metrics. For example, one can use individually noisy and nonlinear amplifiers and low-resolution quantizers to emulate high-performance versions, thus greatly reducing hardware complexity and overall power consumption. As a result, the design and cooling requirements of dense multi-beam arrays can be greatly simplified.

In practice, the available performance improvements due to spatial and spatio-temporal noise-shaping are eventually limited by the increase in mutual coupling between the antenna elements as the spatial oversampling factor K_u increases. Intuitively, a highly-oversampled array approaches a continuous aperture, implying that no further improvements in NF, linearity, or ENOB are possible [85], [86]. However, both simulations and experiments confirm that significant performance benefits are achievable using common antenna elements (e.g., patches and dipoles) for moderate oversampling ratios ($K_u \leq 4$).

IV. Novel Wideband Multi-Beamformers at Low Size, Weight, and Power (SWaP)

We now demonstrate promising new approaches in computation for obtaining beamforming array patterns with much less computation power and time than conventional methods.

An N-element uniformly-spaced linear antenna array can be used to realize an N-beam multi-beamformer by computing N-element discrete Fourier transforms (DFTs) along the spatial dimension. These computations can be efficiently performed using a spatial Fast Fourier transform (FFT), which can be implemented using both analog as well as digital approaches [88] and reduces the brute force computational complexity of the DFT from $\mathcal{O}(N^2)$ down to $\mathcal{O}(N \log N)$. Moreover, approximate versions of the DFT can be computed with even lower complexity than the FFT, as shown by Cintra, Bayer, and their collaborators [89]–[93]. The Cintra-Bayer approach to approximate-DFT computation allows significantly smaller arithmetic complexity over FFT-based approaches (in some cases, reducing the computation burden by an order of magnitude for large N) at the cost of only $\sim$2 dB penalty in worst-case sidelobe level [89]–[93]. Note that while today's mobile devices do not concern themselves with the power savings due to FFT computations (because fidelity of the modulation is vital for bit error rate), the same may not be true for future wireless devices at mm-wave and THz. In fact, the availability of massive channel bandwidths and likely increase in sensitivity to power consumption (e.g., prolonged battery life) may remove the present-day need for perfect fidelity in DFT/FFT processing and making approximate versions attractive [93].

However, both DFT/FFT and approximate-DFT approaches are narrowband digital beamformers and are therefore not suitable for emerging wideband 5G/6G digital arrays [94]. In fact, true time delay (TTD) beamformers are required for achieving electronically-steered wideband RF beams. Unlike phased-array (i.e., DFT-based) beamformers, which are limited to a relatively small fractional bandwidth because of "beam squint" [95], a TTD beamformer achieves frequency independent wideband RF beams as demanded by 5G and impending 6G applications. However, the digital arithmetic complexity required to generate a massive number of TTD beams can be quite staggering compared to the traditional narrowband methods used in digital phased-arrays. Thus, while the use case for generating a large number of TTD digital beams in emerging wireless systems is a strong one, the resulting arithmetic circuit complexity and power consumption often becomes a limiting factor. A novel approach to multi-beam TTD beamforming has been explored, where the delay Vandemonde Matrix (DVM) and its factorization [96], [97], has the potential to significantly lower the net arithmetic complexity of the underlying digital system, well below the brute-force matrix computations required for the direct-computed DVM approach [95]. Extensions to FFT-like algorithms for the case of the multi-beam DVM-based TTD beamformer are the subject of ongoing research. In particular, fast algorithms for DVM factorization have already been found for relatively small N, while more general versions applicable to larger values of N are being actively developed [95]–[97]. What is fascinating to note is that the use of TTD approaches has also found promise in mmWave and THz circulators and duplexers, which are non-linear devices that allow one-way transmission for coupling multiple signals to a single RF port [98]. Thus, it is clear that TTD approaches for

This article has been accepted for publication in a future issue of this journal, but has not been fully edited. Content may change prior to final publication. Citation information: DOI 10.1109/ACCESS.2019.2921522, IEEE Access

both antennas and circulators/duplexers offer great promise in reducing noise and increasing isolation and linearity for future mm-wave and THz electronics as compared to the electronics used in present-day wireless systems [99].

V. Moving to Beyond 5G and above 100 GHz–A new type of channel

The importance of atmosphere absorption effects on the transmission of high frequency signals has long been recognized [100], [101]. At lower frequencies (below 6 GHz), the attenuation of a propagating wave is mainly caused by molecular absorption in free space, which is minimal [102], but at higher frequencies, as the wavelength approaches the size of dust, rain, snow, or hail, the effects of Mie scattering become more severe [6], [103], [104]. The various resonances of oxygen, hydrogen, and other gases in the atmosphere, however, cause certain frequency bands to suffer from significant signal absorption. Fig. 6 illustrates how the frequency bands of 183 GHz, 325 GHz, 380 GHz, 450 GHz, 550 GHz, and 760 GHz suffer much greater attenuation over distance in typical air due to the atmospheric absorption, beyond the natural Friis' free space loss, making these particular bands well suited for very short range and secure communications such as "whisper radio" applications, where massive bandwidth channels will attenuate very rapidly out to a few tens of meters, meters, or fractions of a meter [2], [4], [6], [25], [104]. Fig. 6 also shows many mmWave and THz bands suffer surprising little loss as compared to sub 6-GHz bands, perhaps less than 10 dB/km of additional loss than caused by free space propagation in air. These frequency bands could easily be used for high speed 6G mobile wireless networks with up to km size coverage range, and perhaps even up to 10 km or beyond in fixed applications [4], [25], [105]–[107]. In fact, Fig. 6 shows that at much of the spectrum between 600 and 800 GHz suffers 100 to 200 dB/km attenuation, which is only 10 to 20 dB over a 100 small cell distance. As shown subsequently, high gain electronically steered directional antennas, that are physically small, will easily overcome this atmospheric attenuation, meaning that the mobile industry will be able to work well up to 800 GHz in the future using the small-cell architectures envisioned for 5G.

Work in [108] showed that particles such as rain drops, snow, and hail caused substantial attenuation at frequencies above 10 GHz. 73 GHz signals attenuate at 10 dB/km when the rain rate is 50 mm/h [2], [6], [109]. Interestingly, as shown in [2], [101], [110] rain attenuation flattens out from 100 GHz to 500 GHz, meaning that rain will not cause any additional attenuation at operating frequencies above 100 GHz (see Fig. 7). For all mmWave frequencies where the urban cell sizes are on the order of 200 m, rain or snow attenuation can clearly be overcome with additional antenna gain (obtainable by switching in more antenna array elements) [2], [4], [6].

Work in [102], [111]–[115] showed effects of rain, fog, dust, and air turbulence at THz and infrared frequencies based on measurements with less than 10 m links, which indicated a relatively small change (a few dB) in the received power compared to the power received in clear weather. THz outdoor measurements during a snow fall at 200 GHz were presented in [103], and a 2 dB decrease in the received power was observed across an 8 m LOS link indicating that a higher transmitted power was required during a snow fall to maintain the same data rate. As shown in Fig. 7, mmWave and THz wireless channels are expected to experience $\sim$30 dB/km of rain attenuation above 100 GHz.

Since the first Fresnel zone is tiny at THz frequencies, the antenna beams of wireless devices are easily blocked [116], [117], which requires rapidly steerable phased array transceivers to support both adequate transmission range and to provide adaptive beam steering [2], [8], [60], [110]. The array angular resolution approximates λ/L, where λ is the wavelength at the carrier frequency and L is the aperture of the array. For example, consider a fixed wireless system or mobile base station using a 340 GHz carrier with a 35 cm (14 inch) aperture – this permits a sharp 0.14 $^\circ$ beam resolution [21]. Three system examples – a 140 GHz, 10 Gbps picocell backhaul unit using 64-element arrays; a 340 GHz, 8-channel 160 Gbps MIMO backhaul link with each channel comprised of a 64-element subarray module; and a heads-up-display 400 GHz automotive imaging radar using a linear 64×512 array and frequency scanned beam steering were presented in [60], thus proving the capability of building THz systems.

There is still a recurring misconception among researchers, that the wireless channels at higher frequencies would experience more loss, since they have been taught to only consider the free space path loss (FSPL) with omnidirectional antennas. However, it is important to note that at higher frequencies, the antennas (for a given physical size) will be more directional and have more gain. Friis free space equation (4) with antenna gain (5) readily demonstrate that higher frequency links are viable with less loss, not more [6], [28]. With directional antennas at both link ends, the received power is given by (6). Theoretically, *the path loss in free space decreases quadratically as frequency increases*, so long as the physical size of the antenna (effective aperture) is kept constant over frequency at both link ends [4], [6], [28], [118].

The astounding result of improved coverage at higher frequencies is clear in Fig. 8, where the received power at 140 GHz free space is 5.7 dB and 14 dB greater than the power received at 73 GHz and at 28 GHz, respectively, for the same TX output power and for identical physical antenna areas at all frequencies (see Ch.3 in [6]). The better wireless links at higher frequencies enable wider bandwidths to be used while keeping the same signal to noise ratio as at lower frequencies.

VI. Channel Sounding and Channel Properties Above 100 GHz

There are three main channel sounding techniques in the THz range, namely, THz Time Domain Spectroscopy (THz-TDS), Vector Network Analyzer (VNA) based channel sounding, and correlation based sounding [6], [28], [118]–[121]. THz-TDS is based on sending ultrashort pulsed laser light from a common source to the transmitter (TX) and the receiver (RX). The TX converts the ultrashort light pulse to the THz range and the detector at the RX transforms the received field strength of the THz impulse into an electrical signal when the optical impulse hits the detector [119], [120]. The short

This article has been accepted for publication in a future issue of this journal, but has not been fully edited. Content may change prior to final publication. Citation information: DOI 10.1109/ACCESS.2019.2921522, IEEE Access

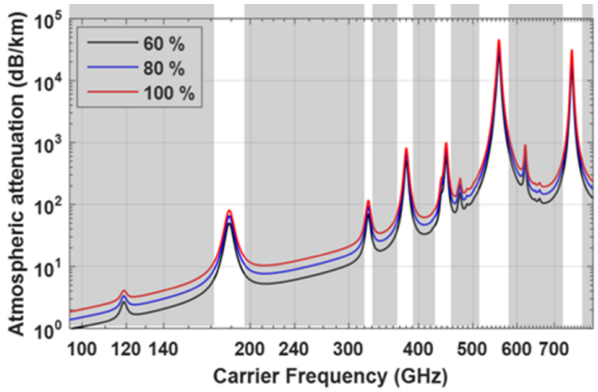

Fig. 6: Atmospheric absorption beyond the natural Friis free space loss of electromagnetic waves at sea level versus frequency under different humidity conditions [101], [104].

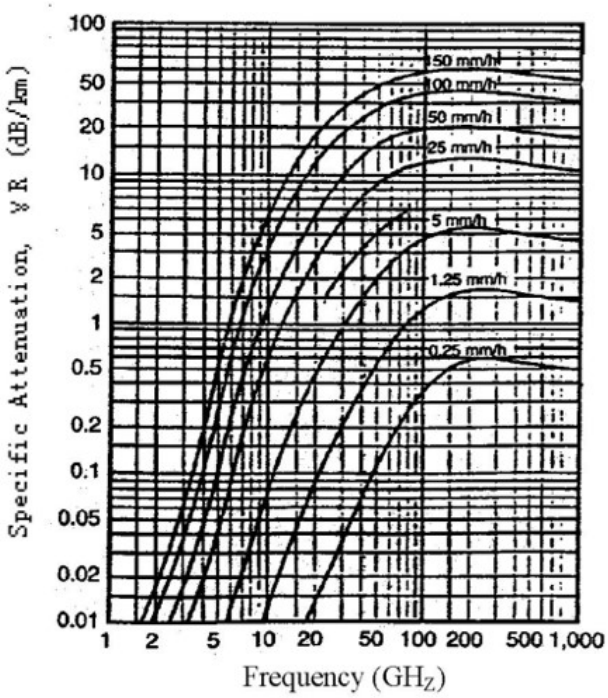

Fig. 7: Rain attenuation flattens out above 100 GHz. The rain attenuation at 1 THz is 10 dB/km for moderate rainfall of 25 mm/h, only 4 dB/km more than the rain attenuation experienced at 28 GHz [2], [101], [110].

THz-TDS pulses cover a huge bandwidth and are excellent for estimating electrical and scattering parameters of sample materials. However, due to the large size of the spectrometer and the limited output power, it is not suitable to be used over a wide range of indoor or outdoor scenarios or for measuring the wireless channels at more than a few meters of distance.

Four-port VNAs are commonly used for THz range channel sounding, where the two additional ports (compared to the traditional two-port VNAs used at lower frequencies) are used to generate a local oscillator for the mixer in the frequency extensions, that are used to elevate the VNA stock frequency range to much higher frequencies through heterodyning [120], [121]. A VNA sweeps discrete narrowband frequency tones across the bandwidth of interest to measure the S_{21} parameter of the wireless channel. Due to the long sweep time across a broad spectrum which can exceed the channel coherence

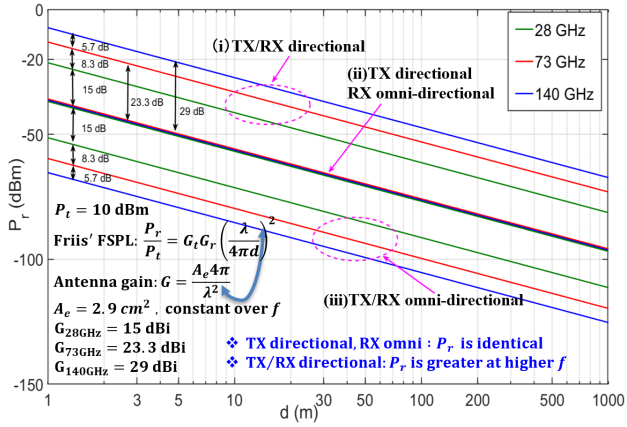

Fig. 8: Received power vs. distance with (i) TX and RX are both directional, (ii) TX is directional but RX is omnidirectional, and (iii) both TX and RX are omnidirectional at 28 GHz, 73 GHz, and 140 GHz. Directional antennas with equal effective aperture (A_e = 2.9 cm^2) at both TX and RX have much less path loss at higher frequencies (see Ch.3 in [6] and [28]).

time, VNA-based channel sounders are typically used in a static environment and require a cable that can be a tripping hazard over tens or hundreds of meters [28], [118], [121].

Correlation based channel sounder systems transmit a known wideband pseudo-random sequence. At the RX, the received signal is cross-correlated with an identical but slightly delayed pseudo-random sequence, providing autocorrelation gain at the expense of a slightly longer acquisition time (on the order of tens of ms) [118], [121], [122]. Sliding correlator chips have recently been produced that offer a 1 Gbps baseband spread spectrum sequence [123], and sliding correlators generally enable cable-free operation over useful mobile communication distances of up to 200 m at sub-THz frequencies, depending on transmit power, bandwidth, and antenna gain [28], [121]. A 140 GHz channel sounder with 1 GHz RF bandwidths has been used to measure indoor channels at NYU [28], with new measurements results given in Section VII. A correlation-based channel sounder at 300 GHz with 8 GHz bandwidth was presented and evaluated in [120] with the same wired clock source being connected to both the TX and RX, which use a subsampling technique to avoid the expense of high-speed A/D converters. A 12th order M-sequence was used with a subsampling factor of 128, and the theoretically maximum measurable Doppler frequency was 8.8 kHz, equivalent to a velocity of 31.7 km/h at 300 GHz [120].

Measurements at 100, 200, 300, and 400 GHz with a 1 GHz RF bandwidth THz-TDS channel sounder showed that both indoor LOS and NLOS (specular reflection from interior building walls) links could provide a data rate of 1 Gbps [104].

Propagation loss measurements for estimating the performance of a communication link in the 350 GHz frequency band were presented in [124], where a VNA based system was used with 26 dBi gain co-polarized horn antennas at both the TX and RX. The presence of water absorption lines in the spectra at 380 GHz and 448 GHz was very evident. Data rates of 1 Gbps for a 8.5 m link and 100 Gbps for a 1 m T-R separation distances were shown to be possible via wireless communication links at 350 GHz [124]. Channel and propagation measurements at 300 GHz were presented in

This article has been accepted for publication in a future issue of this journal, but has not been fully edited. Content may change prior to final publication. Citation information: DOI 10.1109/ACCESS.2019.2921522, IEEE Access

[125], [126], where a VNA based channel system with 26 dBi gain horn antennas at both TX and RX was used to analyze the channel characteristics from 300-310 GHz with an IF frequency bandwidth of 10 kHz. Maximum transmission rates of several tens of Gbps for LOS and several Gbps for NLOS paths were shown to be achievable [126]. THz band indoor propagation measurements were conducted in [127] using a VNA based system covering a frequency range from 260 GHz to 400 GHz with 25 dBi gain horn antennas at both TX and RX within a T-R separation range of 0.95 m. Measurement results showed that Tbps throughput was achievable in the THz band. However, robust beam forming algorithms will be required in THz band communications. Acoustic ceiling panels, which were shown to be good reflectors at THz band, could be used as low cost components to support NLOS links [127].

Absorption coefficients of glass, medium density fiberboard, and plexiglass were measured where the S_{21} parameter was recorded at a T-R separation distance of 10 cm with and without the obstructions brought into the ray path, showing that a 2.5 cm thick window and a 3.5 cm thick fiberboard door would induce absorption attenuation of approximately 65.5 dB and 86.7 dB at 300 GHz [125], respectively. Second generation transceivers demos for D-band radars with Doppler, loop-back, and 4 Gbps NLOS radio links, over the air and at distances exceeding one meter were presented in [128]. The transceiver chip-set operated at 122 GHz based on low-voltage typologies with a 7.5 dB noise figure and -95 dBc/Hz phase noise while consuming only 220 mW.

VII. Comparing 28, 73, and 142 GHz Channels

Propagation measurements in the 140 GHz band were conducted in a shopping mall [129], [130] using a VNA based channel sounder with a 19 dBi horn antenna at the RX, and a 2 dBi bicone antenna at the TX. It was shown that the numbers of clusters and multipath components (MPCs) in each cluster in the 140 GHz band, an average of 5.9 clusters and 3.8 MPCs/cluster, were fewer compared to the 28 GHz band, which had an average of 7.9 clusters and 5.4 MPCs/cluster [129]. Work in [131], [132] presented D-band propagation measurements in a very close-in environment around a personal computer using a VNA based sounder. Indoor directional path losses at 30 GHz, 140 GHz, and 300 GHz were compared using different path loss models in [132]. Although the LOS path loss models predicted path loss exponents (PLE) close to 2.0, the multi-frequency close-in free space reference distance model with a frequency-dependent term (CIF) and alpha-beta-gamma (ABG) model had slightly better PLE and standard deviation stability for the indoor environments than the single-frequency CI and Floating Intercept (FI) models (although a sensitivity analysis such as provided in [133] has not yet been performed for indoor sub-THz channels) [4], [132], [134]–[136].

Indoor channel measurements in the 126-156 GHz frequency band were given in [137] using a VNA-based channel sounder and 20 dBi gain horn antennas at both TX and RX within a T-R separation distance of 10.6 m. The PLE for the measured D band signal was close to 2 (free space) since the LOS component is much stronger than the secondary paths. The root mean square delay spread was found to be 15 ns [137].

Channel modeling and capacity analysis for THz band electromagnetic (EM) wireless nano-networks were explored in [138], where a propagation model accounting for the total path loss and the molecular absorption for EM communications in the THz band (0.1-10 THz) was developed based on radiative transfer theory. Channel capacity of the THz band was investigated by using the proposed path loss model for different power allocation schemes, showing that for several tens of millimeters propagation distance, the THz channel supports very large bit-rates (up to few terabits per second), which enables a radically different communication paradigm for nano-networks [138].

A. Calibration, Free space path loss, and Antenna cross-polarization discrimination

A key to all measurements is using a standard approach for calibration, that assures repeatable measurements by any research team at any frequency [139]. 140 GHz FSPL verification measurements were conducted at T-R separation distances of 1, 2, 3, 4, and 5 m using the standard calibration and verification method taught in [139], and the results are shown after removal of antenna gains in Fig. 10, together with 28 GHz and 73 GHz path loss measurement data [2], [140]. The measured path loss at 140 GHz agrees with Friis FSPL equation [141]. The CI path loss model with 1 m reference distance [2] fits perfectly to the measured data, showing that the CI model is viable well above 100 GHz.

As shown in Fig. 10, the difference in the path loss measured at 73 GHz and 140 GHz in far field distances within a few meters is 5.85 dB, which is extremely close to the theoretical value calculated by Friis FSPL equation ($20 \times 10 \log_{10} \frac{140}{73} = 5.66$ dB), indicating the high accuracy and proper calibration of the channel sounder system. The difference in the path loss between the 28 and 73 GHz measurements at the same distance is 8.45 dB, which is virtually identical to Friis FSPL equation ($20 \times 10 \log_{10} \frac{73}{28} = 8.32$ dB) [139], where calibration and path loss values were calculated using (4)-(6).

$$P_r = \frac{P_t G_t G_r \lambda^2}{(4\pi d)^2} \tag{4}$$

$$G = \frac{A_e 4\pi}{\lambda^2} \tag{5}$$

$$P_r = \frac{P_t A_{et} A_{er}}{d^2 \lambda^2} \tag{6}$$

Polarization diversity can provide up to twice the data rates in dual-polarized communication systems, as compared to single co-polarized systems without any extra bandwidth or spatial separation between antennas [142], [143]. Measurements and calibration for antenna cross-polarization discrimination (XPD) at 28, 73, and 140 GHz were conducted to analyze the polarization characterization of the horn antennas [139], [144]. The XPD values also are required to analyze the polarization effects of partitions at different frequencies.

The architectures of the channel sounders used in the measurements given here have been extensively described in [28], [121]. The LO, IF frequencies, and antenna characteristics are summarized in Table III. The output power from the TX

This article has been accepted for publication in a future issue of this journal, but has not been fully edited. Content may change prior to final publication. Citation information: DOI 10.1109/ACCESS.2019.2921522, IEEE Access

TABLE III: Summary of NYU channel sounder systems and antennas used in measurements at 28 GHz, 73 GHz and 142 GHz [2], [28], [121]

RF Frequency	LO Frequency	IF Frequency	RF Bandwidth	Antenna HPBW	Antenna Gain	Antenna XPD	A_e
28 GHz [2]	22.6 GHz	5.4 GHz	1 GHz	30°	15 dBi	19.30 dB	2.88 cm^2
73 GHz [121]	67.875 GHz	5.625 GHz	1 GHz	15°	20 dBi	28.94 dB	1.32 cm^2
142 GHz [28]	135 GHz	7 GHz	4 GHz	8°	27 dBi	44.18 dB	1.83 cm^2

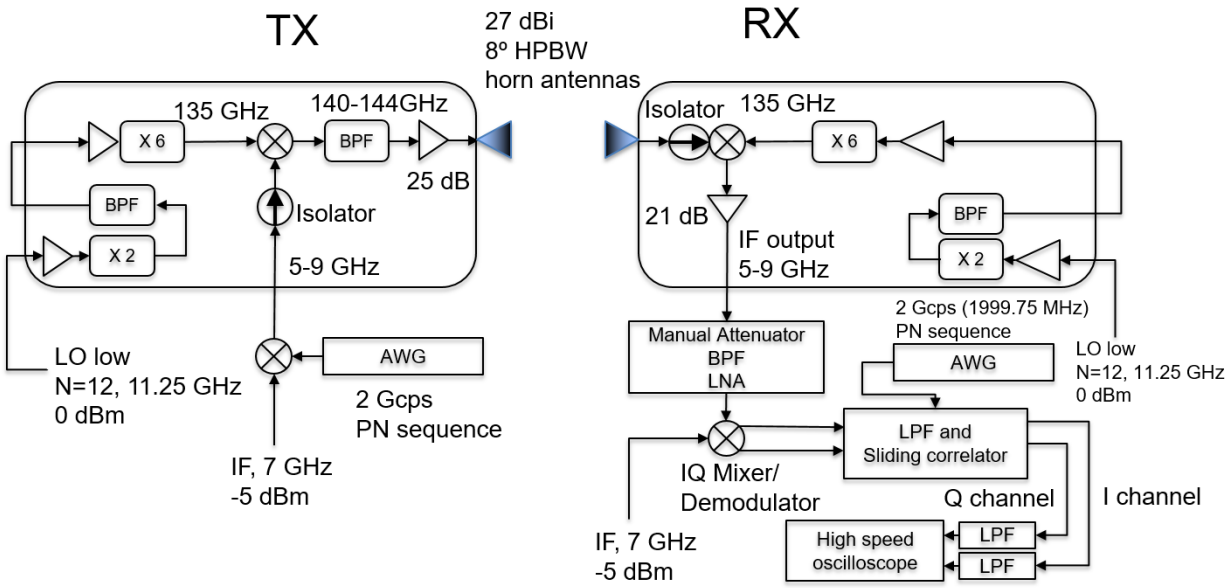

Fig. 9: Block diagram of 140 GHz broadband channel sounder system with 4 GHz 3 dB RF bandwidth used at NYU WIRELESS.

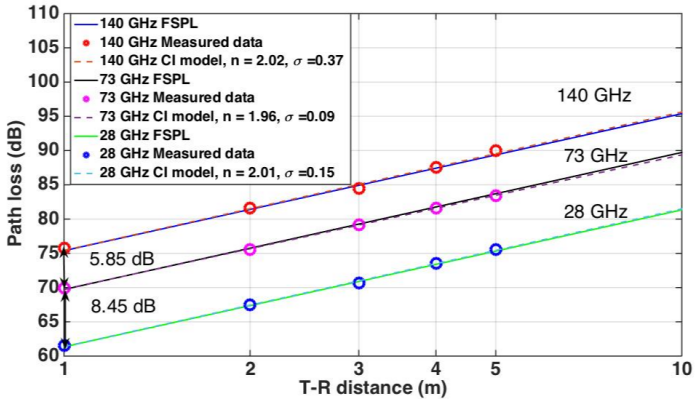

Fig. 10: 28, 73 and 140 GHz free space path loss (after subtracting out all antenna gains) verification measurements at distances of 1, 2, 3, 4, and 5 m.

waveguide (with the antenna removed) was measured using a PM5-VDI/Erickson Power Meter having a highly accurate power resolution of 10^{-4} mW.

To properly calibrate our measurements, FSPL measurements at 28, 73, and 140 GHz were firstly conducted at 3, 3.5, 4, 4.5, and 5 m, according to the reference procedures introduced in [139], with vertically polarized 27 dBi gain horn antennas at both the TX and RX. The FSPL measurement results after removing the antenna gains are shown in Fig. 8, indicating a negligible difference (less than 0.5 dB) from the theoretical Friis FSPL equation over all distances, which validates the accuracy of the channel sounder.

After the free space power measurements with co-polarized antennas, measurements were conducted at the same distances but with cross-polarized antennas (e.g., V-H). Cross-polarization was realized by using a waveguide twist which rotates the antenna by 90°. The insertion loss caused by the twist was measured and calibrated out. The received power for the cross-polarized antennas is shown in Fig. 11. The XPD was calculated by taking the difference between the path losses of the V-V and V-H antenna configurations at same distances. See [139] for a detailed description of the XPD verification and calibration procedure used, that can be universally applied. Note that at a fixed TR separation distance, the free space received powers for the H-H and H-V configurations were within 1 dB of the V-V and V-H received powers, respectively, showing reciprocity with cross-polarization measurements.

B. mmWave and THz Partition Loss Measurements

Wideband mmWave and THz networks, as well as precise ray-tracer algorithms [154], [155], will require accurate channel models that accurately represent the partition losses induced by common building objects [53], [139]. Therefore, partition loss of common building materials needs to be extensively investigated for 5G mmWave wireless systems and future THz wireless communications in and around buildings.

Partition loss measurements at 2.5 and 60 GHz of a variety of materials like drywall, office whiteboard, clear glass, mesh glass, using a wideband channel sounder with vertically polarized antennas at both TX and RX were presented in [147], where root mean square (RMS) delay spreads were found to

This article has been accepted for publication in a future issue of this journal, but has not been fully edited. Content may change prior to final publication. Citation information: DOI 10.1109/ACCESS.2019.2921522, IEEE Access

TABLE IV: Partition Loss of Common Outdoor materials

Material	Material Thickness	Average Attenuation	Standard Deviation	Frequency	Polarization	Ref.
Brick Pillar	185.4 cm	28.3 dB	–	28 GHz	V-V	[145]
Brick Wall	–	12.5 dB	2.4 dB	5.85 GHz	V-V	[146]
	–	16.4 dB	3.3 dB	5.85 GHz	V-V	[146]
Cinderblock Wall	–	22.0 dB	3.5 dB	5.85 GHz	V-V	[146]
Wood siding exterior	–	8.8 dB	3.5 dB	5.85 GHz	V-V	[146]
Tinted Glass	3.8 cm	40.1 dB	–	28 GHz	V-V	[145]
	1.2 cm	24.5 dB	–	28 GHz	V-V	[145]
Mesh Glass	0.3 cm	7.7 dB	1.4 dB	2.5 GHz	V-V	[147]
	0.3 cm	10.2 dB	2.1 dB	60 GHz	V-V	[147]

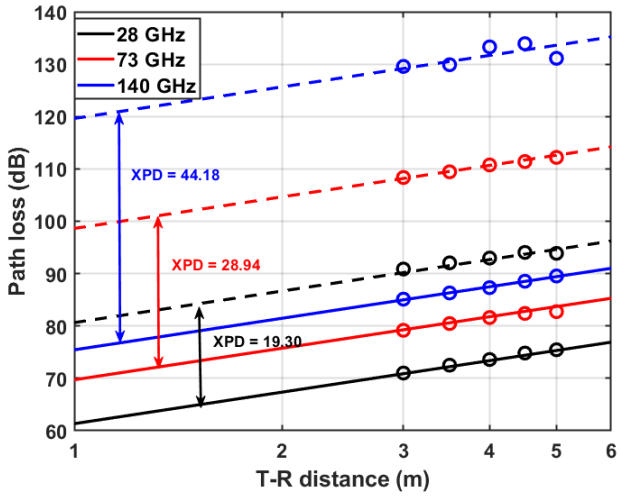

Fig. 11: Measured antenna XPD at 28, 73, and 140 GHz. The solid lines and the dash lines represent the path loss measured with co-polarized and cross-polarized antennas, respectively. The XPD values calculated across five distances are within 1 dB at each frequency, which verifies the XPD measurement procedure is correct.

be much lower at 60 GHz than at 2.5 GHz. Based on the measured data, a partition-based path loss model which provided fast and accurate link budget predictions in a multipath-rich environment was developed in [146], [147]. Partition loss measurements at 73 GHz for V-V and V-H polarization configurations for glass doors, drywall, steel doors, and clear glass were conducted in [148]. The co-polarized partition loss for glass doors and windows was found to be 5-7 dB at 73 GHz, and steel doors induced a partition loss as large as 40-50 dB, showing that different materials could be properly chosen for propagation or interference isolation between neighboring rooms [28], [139], [148]. The partition loss of common outdoor and indoor materials are summarized in Table IV and V, respectively, and reveal that not much is known above 100 GHz.

Effective attenuation of typical building materials such as concrete bricks, wood, tiles, and a gypsum plate were measured at 100 GHz with the TX and RX boresight-aligned [153]. The co-polarization situations (both TX and RX were vertically or horizontally polarized) were analyzed, and the effective attenuation of most of the building materials was observed to be polarization sensitive [153].

Work in [150] presented penetration loss measurements of concrete walls and plasterboard walls over the frequency range of 900 MHz to 18 GHz, as shown in Table V, and the penetration loss was shown to not necessarily increase monotonically with respect to frequency. A comparison of measured partition loss versus frequency for a variety of different common building materials was shown in [151].

As measured in [151], an 8-inch concrete wall had a typical partition loss of 2 to 4 dB at 900 MHz for both V-V and H-H antenna configurations. The attenuation through solid wood, having a thickness of 2 cm, was measured to be about 5 dB and 8 dB at 45 GHz for both H-H and V-V antenna configurations, respectively, while the attenuation through a concrete slab having a thickness of 3 cm was measured to be about 13 dB at 45 GHz for both H-H and V-V antenna configurations [152]. Penetration loss measurements in THz band (0.1 - 10 THz) of plastic board, paper, and glass which had losses of 12.47 dB/cm, 15.82 dB/cm, and 35.99 dB/cm were presented in [149]. However, the measurements in [149] were conducted in a very short range (less than 10 cm) and the thicknesses of sample materials were less than 1 cm which may cause large uncertainty or error.

Absorption coefficients of glass, medium density fiberboard, and plexiglass were measured where the S_{21} parameter was recorded at a T-R separation distance of 10 cm with and without the obstructions brought into the ray path, showing that a 2.5 cm thick window and a 3.5 cm thick fiberboard door would induce absorption attenuation of approximately 65.5 dB and 86.7 dB at 300 GHz [125], respectively.

Partition loss measurements at 28, 73, and 140 GHz were conducted at the NYU WIRELESS research center. T-R separation distances of 3, 3.5, 4, 4.5, and 5 m were used and the TX/RX antenna heights were 1.6 m (see Fig. 3 in [139]). These distances are greater than $5 \times D_f$, where D_f is the Fraunhofer distance to ensure a plane wave is incident upon the measured material, and the dimensions of the measured materials are large enough such that the radiating wavefront from the TX antenna is illuminated on the material without exceeding the projected HPBW angle spread from the TX antenna [139]. At each distance, five measurements/power delay profiles (PDP) were recorded with slight movements on the order of half a wavelength, taking the average of the power in the first arriving

This article has been accepted for publication in a future issue of this journal, but has not been fully edited. Content may change prior to final publication. Citation information: DOI 10.1109/ACCESS.2019.2921522, IEEE Access

TABLE V: Partition Loss of Common Indoor Materials

Material	Thickness (cm)	Attenuation (dB)	std (dB)	Frequency	Polarization	Ref.
Drywall	2.5	5.4	2.1	2.5 GHz	V-V	[147]
	2.5	6.0	3.4	60 GHz	V-V	[147]
	38.1	6.8	—-	28 GHz	V-V	[145]
	13.3	10.6	5.6	73 GHz	V-V	[148]
	13.3	11.7	6.2	73 GHz	V-H	[148]
	14.5	15.0	–	140 GHz	V-V	[28]
Clear Glass	0.3	6.4	1.9	2.5 GHz	V-V	[147]
	1.2	3.9	–	28 GHz	V-V	[145]
	1.2	3.6	–	28 GHz	V-V	[145]
	0.3	3.6	2.2	60 GHz	V-V	[147]
	0.6	8.6	1.3	140 GHz	V-V	[28]
	1.3	16.2	–	140 GHz	V-V	[28]
	2.5	86.7	–	300 GHz	V-V/H-H	[28]
	0.16-0.48	15-26.5	–	0.1-10 THz	V-V	[149]
Steel Door	5.3	52.2	4.0	73 GHz	V-V	[148]
	5.3	48.3	4.6	73 GHz	V-H	[148]
Office Whiteboard	1.9	0.5	2.3	2.5 GHz	V-V	[147]
	1.9	9.6	1.3	60 GHz	V-V	[147]
Heavily reinforced uniform concrete wall	35.0	22.0	–	1-4 GHz	V-V	[150]
	35.0	35.0	–	6 GHz	V-V	[150]
	35.0	64.0	–	9 GHz	V-V	[150]
Slightly reinforced uniform concrete wall	20.3	2.0-4.0	–	900 MHz	V-V/H-H	[151]
	12.0	8.0	–	1-3 GHz	V-V	[150]
	12.0	13.0	–	3-7 GHz	H-H	[150]
	12.0	17.0	–	5 GHz	V-V	[150]
	12.0	27.0	–	10 GHz	V-V	[150]
	12.0	32.0	–	8-12.0 GHz	H-H	[150]
	12.0	27.0	–	15 GHz	V-V	[150]
	12.0	23.0	–	12-18 GHz	H-H	[150]
Concrete slab	3.0	13.1	–	45 GHz	H-H	[152]
	3.0	13.9	–	45 GHz	V-V	[152]
Solid wood	2.0	4.8	–	45 GHz	H-H	[152]
	2.0	8.4	–	45 GHz	V-V	[152]
	2.0	19.0	–	100 GHz	H-H	[153]
	2.0	20.4	–	100 GHz	V-V	[153]
	4.0	41.6	–	100 GHz	V-V	[153]
	3.5	65.5	–	300 GHz	V-V/H-H	[125]
	0.25-0.75	14.0-26.0	–	0.1-10 THz	V-V	[149]
Cement tile	2.5	39.5	–	100 GHz	H-H	[153]
	2.5	39.3	–	100 GHz	V-V	[153]
Gypsum board	1.2	3.5	–	100 GHz	–	[153]
Plastic	0.2-1.2	8.0-20.0	–	0.1-10 THz	–	[149]
Paper	0.25-1.0	12.0-24.0	–	0.1-10 THz	–	[149]
Uniform plasterboard wall	12.0	4.0	–	1-3 GHz	V-V	[150]
	12.0	10.0	–	5 GHz	V-V	[150]
	–	4.7	2.6	5.85 GHz	V-V	[146]
	12.0	6.0	–	6-7 GHz	V-V	[150]
	12.0	18.0	–	15 GHz	V-V	[150]
	12.0	11.0	–	18 GHz	V-V	[150]

This article has been accepted for publication in a future issue of this journal, but has not been fully edited. Content may change prior to final publication. Citation information: DOI 10.1109/ACCESS.2019.2921522, IEEE Access

TABLE VI: Partition Loss Measurement Results at 28, 73, and 140 GHz for Clear Glass

Pol.	28 GHz		73 GHz		140 GHz	
	Mean (dB)	STD (dB)	Mean (dB)	STD (dB)	Mean (dB)	STD (dB)
V-V	1.53	0.60	7.17	0.17	10.22	0.22
V-H	20.63	1.32	37.65	0.53	46.92	2.05
H-V	22.25	0.88	36.92	1.11	37.37	1.79
H-H	1.48	0.54	7.15	0.44	10.43	0.55

TABLE VII: Partition Loss Measurement Results at 28, 73, and 140 GHz for Drywall

Pol.	28 GHz		73 GHz		140 GHz	
	Mean (dB)	STD (dB)	Mean (dB)	STD (dB)	Mean (dB)	STD (dB)
V-V	4.15	0.59	2.57	0.61	8.46	1.22
V-H	25.59	2.85	24.97	0.58	27.28	1.77
H-V	25.81	0.65	23.38	0.65	26.00	1.42
H-H	3.31	1.13	3.17	0.68	9.31	0.61

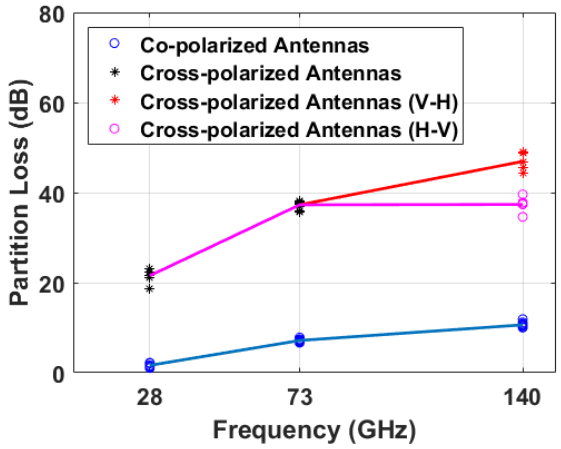

Fig. 12: Partition loss measurement results of clear glass with a thickness of 1.2 cm at 28, 73, and 140 GHz. Partition loss trends to increase with frequencies for both co-polarized and cross-polarized antenna configurations.

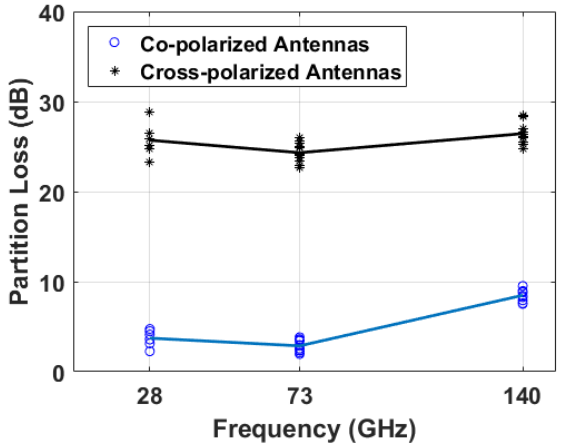

Fig. 13: Partition loss measurement results of drywall with a thickness of 14 cm at 28, 73, and 140 GHz.

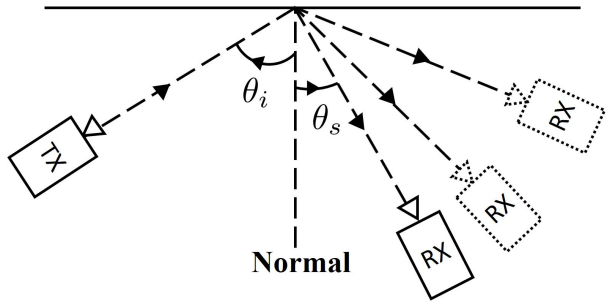

Fig. 14: Setup for scattering measurements. θ_i is the angle the incident ray makes with the normal and θ_s is the scattered angle.

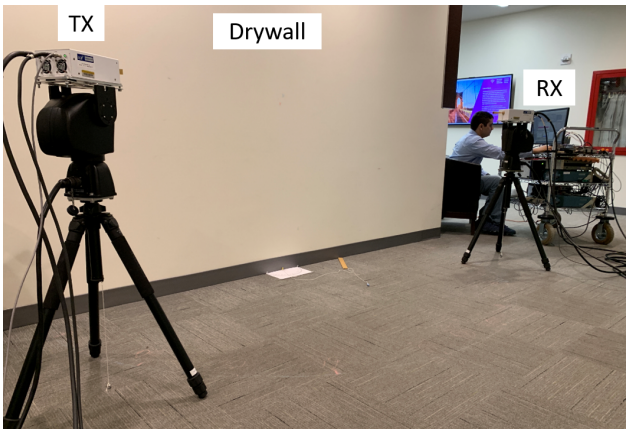

Fig. 15: Photograph of the scattering measurement setup. The scattered power of drywall was measured at a distance 1.5 m away from the wall, in angular increments of 10°.

multipath component of the recorded PDPs, to exclude the multipath constructive or destructive effects. With 4 GHz RF bandwidth, the channel sounder systems used in this paper have a time resolution of 0.5 ns, which means any multipath components spaced more than 0.15 m in propagation distance can be resolved [28].

The partition loss results of common building construction materials, drywall and clear glass, at 28, 73 and 140 GHz, were listed in Table VI and Table VII. The mean partition loss of clear glass at 28 GHz for co-polarized situation (V-V and H-H), see Table VI, was about 1.5 dB with a standard deviation (std) of 0.5 dB. But the same glass had greater partition losses of 7.17 dB and 10.22 dB at 73 GHz and 140 GHz, respectively, for the co-polarization situation.

It is worth noting that the XPD has not been subtracted from the cross-polarized partition loss measurements shown in Table VI and Table VII. Subtracting the XPD results in a negative value of partition loss due to the polarization coupling effects (depolarization) of the building materials. It is shown in Fig. 12 and 13 that the partition loss tends to increase with frequencies for both co-polarized and cross-polarized antenna configurations.

VIII. Scattering above 100 GHz

Scattering at mmWave and THz frequencies is an important propagation mechanism [6], [62]. The surfaces of buildings, terrain, walls, and ceilings have usually been assumed to be electrically smooth since their surface height variations are small compared to the carrier wavelength at lower frequencies

This article has been accepted for publication in a future issue of this journal, but has not been fully edited. Content may change prior to final publication. Citation information: DOI 10.1109/ACCESS.2019.2921522, IEEE Access

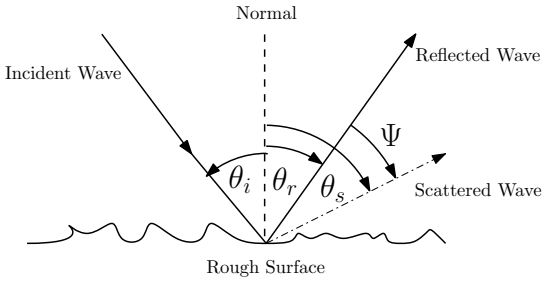

Fig. 16: A radio wave incident at an angle θ_i with respect to the normal to the targeted rough surface. θ_r and θ_s are reflected and scattered angle, respectively. From Snell's law, reflections obey $\theta_i = \theta_r$. Ψ is the angle between reflected and scattered waves.

(e.g., greater than 5 cm at below 6 GHz) [156]. At today's sub-6 GHz cellular and WLAN systems, the reflection process is dominated by a strong specular path at an angle of reflection equal to the angle of incidence, and scattering, being a weaker propagation phenomenon, is negligible. However, in mmWave bands and above, the roughness of surfaces are comparable to the carrier wavelength and the illuminated scatterers may actually create signal paths that are as substantial as, or even stronger than reflected paths, depending on the incident angle [6], [62], [156].

A. Directive Scattering model

The directive scattering (DS) model is widely used to predict the scattered power in optics [157]. The single lobe DS model [158], [159] assumes that the main scattering lobe is steered in the direction of the specular reflection (θ_r shown in Fig. 16). The DS model has been used in [159] to model the RF propagation environment of a hospital room at 60 GHz. The PDP of the environment agreed well with simulations using the DS model, up to an excess delay of 30 ns. The DS model has also been tested at 1.296 GHz in [158], where the DS model agreed with the scattering from rural and suburban buildings. When an electromagnetic wave impinges upon a surface at an incident angle θ_i, the scattered electric field at any particular scattering angle θ_s can be calculated using the DS model. The DS scattered electric field in the incident plane is given by:

$$\begin{aligned} |\mathbf{E}_s|^2 &= |\mathbf{E}_{s0}|^2 \cdot \left(\frac{1+\cos(\Psi)}{2}\right)^{\alpha_R} \\ &= \left(\frac{SK}{d_t d_r}\right)^2 \frac{l\cos\theta_i}{F_{\alpha_R}} \cdot \left(\frac{1+\cos(\Psi)}{2}\right)^{\alpha_i} \end{aligned} \tag{7}$$

where $\mathbf{E}_s$ is the scattered electric field at the scattering angle Ψ. $\mathbf{E}_{s0}$ is the maximum scattered electric field, which is adopted from an effective roughness model [158]. K is given by $\sqrt{60 P_t G_t}$ which is a constant depending on the transmitted power and the transmitter antenna gain [160]. d_t and d_r are the distances between the scatterer and the transmitter and receiver, respectively. l is the length of the scattering object. Ψ is the angle between the reflected wave and the scattered wave, as shown in Fig. 16. α_R determines the width of the scattering lobe with higher values of α_R implying a narrower scattering lobe.

The received power at the receiver can then be calculated as [118]:

$$P_r = P_d A_e = \frac{|\mathbf{E}_s|^2}{120\pi} \cdot \frac{G_r \lambda^2}{4\pi} = \frac{|\mathbf{E}_s|^2 G_r \lambda^2}{480\pi^2} \tag{8}$$

where P_d is the power flux density of the scattered wave, and A_e is receiver antenna aperture [118]. G_r is the receiver antenna gain, and λ is the wavelength of the radio wave. The scattered power is calculated using (7)-(8), and the reflected power is calculated using:

$$\Gamma_{\text{rough}} = \rho_s \cdot \Gamma_{\text{smooth}}, \tag{9}$$

where ρ_s is the scattering loss factor and

$$\rho_s = \exp\Big[-8\left(\frac{\pi h_{\text{rms}} \cos\theta_i}{\lambda}\right)^2\Big] I_0\Big[8\left(\frac{\pi h_{\text{rms}} \cos\theta_i}{\lambda}\right)\Big], \tag{10}$$

where I_0 is the zero-order Bessel function of the first kind. When θ_i = 1°, 30°, and 45° (small incident angles), it was shown in [62] that *the maximum scattered power (in the reflection direction as in Snell's law) computed by the DS model is stronger than the reflected power obtained from the rough surface reflection model for a rough surface*.

Simulations were performed using three materials with incident angle θ_i ranging from 10° to 90°and over frequencies from 1 GHz to 1 THz [62]. It was shown that as the frequency increases, the received scattered power increases, which can be expected since the surfaces tend to be rough as the frequency increases and rougher surfaces cause greater scattered power (even greater than the reflected power). Moreover, the maximum scattered power is received when the incident wave impinges upon the surface along the normal direction. The scattered power falls off sharply when the incident wave becomes grazing, and most of the incident power is reflected [62].

The single lobe DS model may be modified to incorporate power an additional back-scatter lobe [158]. The DS scattered electric field taking into account for backscattering is given by:

$$\begin{aligned} |E_s|^2 = |\mathbf{E}_{s0}|^2 \Bigg[&\Lambda \cdot \left(\frac{1+\cos(\Psi)}{2}\right)^{\alpha_R} \\ &+ (1-\Lambda) \cdot \left(\frac{1+\cos(\Psi_i)}{2}\right)^{\alpha_R} \Bigg] \end{aligned} \tag{11}$$

where Ψ_i is the angle between the scattered ray and the incident ray and Λ determines the relative strength of the back scattered lobe with respect to the main scattered lobe.

B. Scattering Measurements and Results

A smooth metal plate or a conformal metal foil attached on the wall (having a size much larger than the radius of first Fresnel zone for frequencies of 100, 200, 300, and 400 GHz) was shown to provide 6-10 dB more power from specular reflection (at an incident angle of 50°) than the bare painted cinderblock wall did [104], indicating that the effect of scattering from the rough surface was significantly smaller than the effect of absorption from the bare painted cinderblock wall, even at 400 GHz. Specular reflection loss with varied incident angles

This article has been accepted for publication in a future issue of this journal, but has not been fully edited. Content may change prior to final publication. Citation information: DOI 10.1109/ACCESS.2019.2921522, IEEE Access

measurements at 400 GHz were also conducted in [104] with 5 different incident angles ranging from 20° to 60° which showed that when the incident angle is large, reflection loss is small (absorption loss plus the scattering loss) and the scattering loss is negligible. However, when the incident angle is small (e.g., incident ray impinges the wall perpendicularly), the scattering loss is not negligible (4 dB difference than predicted result when scattering losses are neglected) [104].

Scattering measurements at 60 GHz were presented in [156] using a 2 GHz wide baseband sounder to measure the non-specular diffuse scattering with an incident angle of 15°, 30°, and 45°. Two types of building materials were used: a red stone wall (a rough wall surface) and a concrete pillar (a smooth wall surface). The received power was measured in the range of 0° to 90° from the normal to the wall and the term of power concentration was defined as the angular span corresponding to 90% of the received power. It was shown that the angular span is centered at the incident angle and higher incident angles lead to smaller angular spread [156]. The power concentration of the rough wall surface was shown to be significantly larger than the case of a smooth wall surface and the coupling effects (depolarization) is more severe when reflecting/scattering from rough wall surface [156].

Scattering measurements of a drywall were conducted at 142 GHz using the channel sounder system summarized in Table III, and the measurement setups and photos are shown in Fig. 14 and 15. During the scattering measurements, both the heights of TX and RX were set at 1.2 m on an arc with a radius of 1.5 m. Incident angles of 10°, 30°, 60°, 80° were chosen to study the scattering performance from a small incident angle to a large angle with respect to the normal. The RX power was measured in the same plane of the incident ray and the normal of the surface from 10°to 170°in 10°/step (0°and 180°are not able to measure due to the physical size of the channel sounder system).

The path loss is calculated by:

$$\begin{aligned}\text{PL[dB]} =& P_{\text{TX}}[\text{dBm}] - P_{\text{RX}}[\text{dBm}] + G_{\text{TX}}[\text{dBi}] \\ &+ G_{\text{RX}}[\text{dBi}],\end{aligned} \tag{12}$$

where P_{TX} [dBm] is the true transmit power in dBm, P_{RX} [dBm] is the record received power by the channel sounder system, G_{TX} [dBi] and G_{RX} [dBi] are the TX and RX antenna gain in dB, respectively. The scattered loss (SL) was then normalized with respect to the FSPL:

$$\text{SL} = \text{PL[dB]} - \text{FSPL}(f, d)[\text{dB}], \tag{13}$$

$$\text{FSPL}(f, d)[\text{dB}] = 32.4 + 20\log_{10}(f) + 20\log_{10} d, \tag{14}$$

where f is the carrier frequency in GHz and d is the TR separation distance in meter.

Measured scatter patterns of different incident angles at 142 GHz are shown in Fig. 17. The peak scattered power (scattered plus reflected) was observed at the specular reflected angle (Snells law), and peak scattered power was greater at large incident angles than at small incident angles (9.4 dB difference between 80° and 10°, where most of the energy is due to reflection and not scattering). At all angles of incidence, measured power is within 10 dB below the peak power in a ± 10° angle range of the specular reflection angle, likely a function of antenna patterns. In addition, back scattered are also observed (negative RX angles) when the incident angle is small (e.g., 30°and 10°) but was more than 20 dB below the peak received power,which means that the surface of drywall can be modeled as smooth surface at 140 GHz and the reflected power can be used to estimate the received power in the specular reflection direction, especially close to grazing.

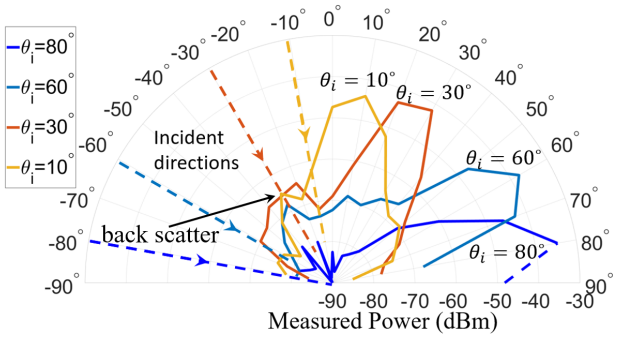

Fig. 17: Polar plots of the scattered power off drywall, measured at four incident angles. Power at scattered angles is measured in 10° increments

A comparison between measurements and predictions made by the dual-lobe DS model (11) with TX incident angle θ_i= 10°, 30°, 60°, and 80° is shown in Fig. 18. It is shown that the peak received power of the simulation at the secular reflection angle agrees well with the measured data (within 2 dB). The received power (measured and simulated) changes versus the RX pointing angle (θ_r as shown in Fig. 14). A back-scattered peak is observed in both the measurement data and the dual-lobe DS model prediction for all the incident angles, and the back-scattered power could be used for imaging around the corner [50], [58].

IX. User Localization in High Frequency Bands

Positioning is the determination of the location of a user that is fixed or moving, based on the known locations of other base stations (BSs). Although users can be localized to within 4.9 m under open sky [161] by the global positioning system (GPS), in obstructed environments such as urban canyons and indoors, the positioning accuracy of GPS is poor. In such environments, 3D maps of the environment along with accurate ToF and angle of arrival (AoA) measurements could be leveraged for precise positioning.

A. ToF and Phase-Based Positioning

In LOS environments, the ToF of a signal can be used to estimate the TR separation distance d (since $d = c \cdot t$ where c is the speed of light and t is the ToF). The RX's position may then be estimated by trilateration. In NLOS environments, ranging introduces a positive bias in the position estimates since the path length of reflected multipath rays is longer than the true distance between the user and the BS.

The ultra-wide bandwidths available at THz frequencies, allow the RXs to resolve finely spaced multipath components and accurately measure the signal's ToF. In [162], the phase of the received signal in LOS was used to estimate the TR separation distance at 300 GHz. By tracking the base-band

This article has been accepted for publication in a future issue of this journal, but has not been fully edited. Content may change prior to final publication. Citation information: DOI 10.1109/ACCESS.2019.2921522, IEEE Access

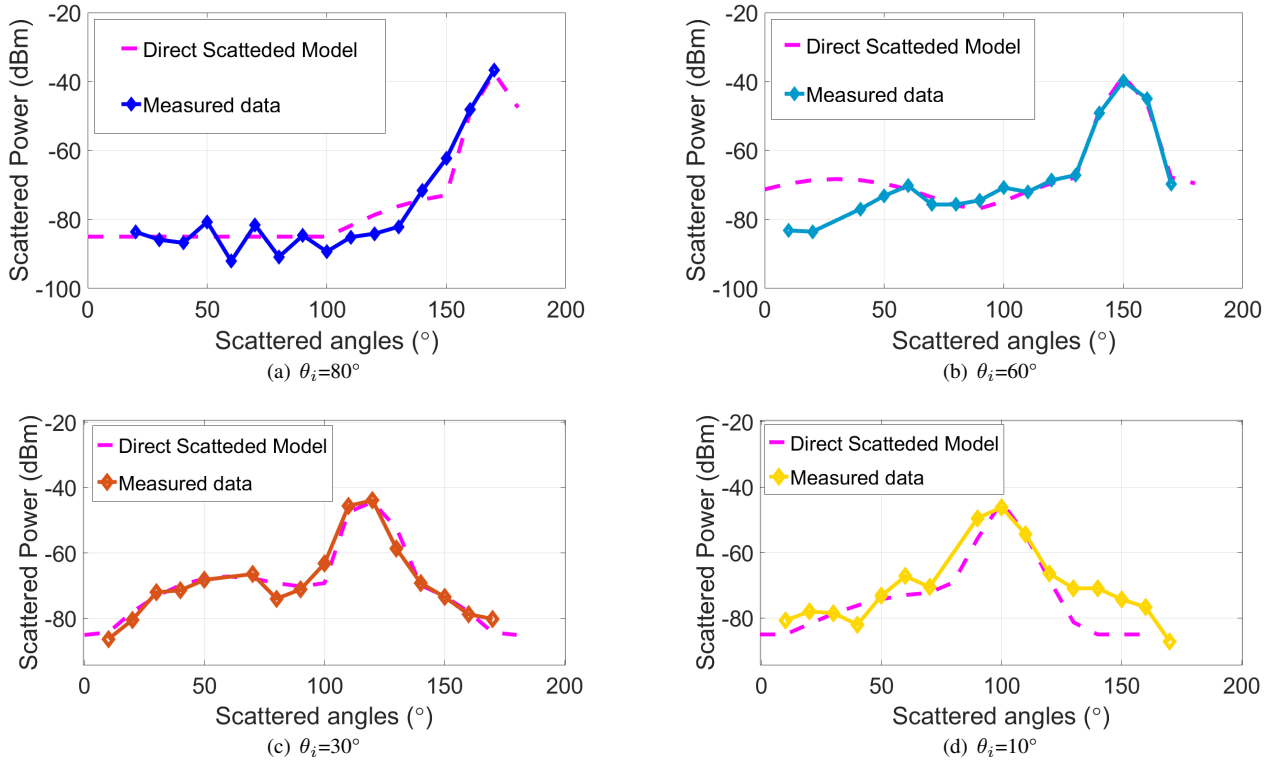

(a) θ_i=80° (b) θ_i=60°

(c) θ_i=30° (d) θ_i=10°

Fig. 18: Comparison between measured data and the dual-lobe Directive Scattering model with TX incident angle θ_i= 80°, 60°, 30°, and 10°at 142 GHz.

modulated signal's phase at the RX and manually correcting for phase ambiguity, decimeter-level accuracy was achieved up to a distance of 40 m [162].

To get the absolute ToF, synchronization is required between the TX and RX, which is not easy in a large network of nodes widely separated. A timing error of 1 ns may result in a positioning error of 30 cm, if no correction for clock bias or clock drift is applied. It is easier for the RX to measure the time-difference-of-arrival (TDoA) of signals arriving from multiple synchronized TXs. In order to determine the relative time delays between the signals, cross-correlation is done. The peaks in the cross-correlation function correspond to the signal propagation time delay.

B. Angle Based Positioning

The line of bearing to the BS is given by the AoA of the signal at the user. The user is localized to the point of intersection of the lines of bearing from several BSs, as seen in Fig. 19. In NLOS environments, due to specular reflections off walls and metallic surfaces, rays do not arrive from the direction of the BS, leading to accuracy penalties [53].

The AoA of the signal is found from detecting the maximum amplitude of the received signal as a function of angular direction. Many methods, such as a sum and difference method used in radars or optical receivers [163] or peak power method may be used. In [53], [164], the angle at which maximal power was received was determined to be the AoA. Alternatively, an antenna array may be used to estimate the AoA, by beamforming and subspace based methods [165]. The Cramer-Rao lower bound (CRLB) is a bound on the minimum variance

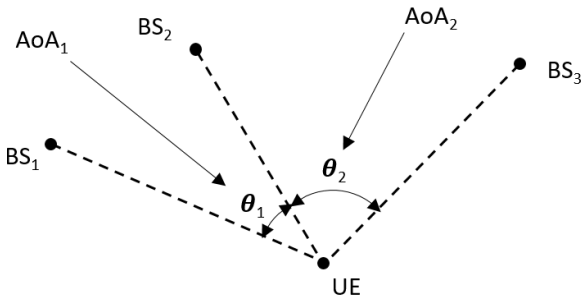

Fig. 19: The UE measures the relative AoAs, θ_1 and θ_2 from BS_1, BS_2, and BS_3. Narrow antenna beamwidths at THz frequencies facilitate accurate AoA measurements

of an unbiased estimate of a parameter. An increase in the number of antenna array elements leads to greater angular resolution and thus a reduction in the CRLB for estimating AoA [166].

C. NYURay - a 3D mmWave Ray Tracer

Ray tracing can be done to simulate channel characteristics at different locations. By using a ray tracer that replicates measured data with high accuracy, costly and time-intensive measurement campaigns can be avoided. Ray tracing allows researchers to test positioning algorithms. In addition, ray tracers can be used to create a radio map of an environment, which could replace the off-line stage of fingerprinting algorithms.

Building on the 2-D mmWave ray tracer developed in [53], NYURay, a 3-D mmWave ray tracer has been developed. NYURay is a hybrid ray tracer which combines shooting-

This article has been accepted for publication in a future issue of this journal, but has not been fully edited. Content may change prior to final publication. Citation information: DOI 10.1109/ACCESS.2019.2921522, IEEE Access

bouncing ray (SBR) based ray tracing with geometry based ray tracing [58].

D. Map-based localization

Work in [50] demonstrated how ToF, AoD measurements, along with a map of the obstacles encountered by the signal could be used to localize a user as described in Section II-D. However, [50] assumes that all materials act like mirrors. The measurements described in Section VII illustrate that at 140 GHz, the partition loss through glass and dry wall is close to 10dB, indicating that materials do not act like perfect reflectors at mmWave and THz frequencies.

The authors of [167] used ToF and an indoor map for localization, using the principal of "virtual access points" to get additional anchor points to localize users that are in NLOS. However [167] does not use AoA information, which will be available with high accuracy using directional antennas at THz frequencies.

In [168], authors used backwards ray tracing using AoA and power observations to estimate the TX location. The transmitted signal had a power of 30 dBm and a bandwidth of 300 MHz. A thermal noise floor of -85 dBm was assumed. Assuming perfect AoA resolution, TXs were localized to within 5 m, 90 % of the time, using six RX locations.

E. Map-assisted Localization with a single BS

Map-assisted positioning with angle and time (MAP-AT) is a novel map-assisted localization technique that shall now be presented. MAP-AT may be used when at least two multipath components arrive at the user. The user need not be in LOS of the BS. The user may either be the TX or the RX of a known radio signal. If the user is a TX, ToF and AoA information is required. If the user is an RX, ToF and AoD information is required. In combination with a 3-D map of the area, the location of the user can be determined.

First consider the case where the user is an RX. If the ToF and AoD of the ray that reaches the user is known and if the ray reaches the user either directly from the BS or through one reflection or by passing through one obstruction, there are two possible locations of the user. If the ray reached the user after one reflection, the BS and user must lie on the same side of the reflecting object. If the ray reached the user directly from the BS, or through one obstruction, the BS and user must lie on a straight line joining the BS and user. The possible locations of the user, based on ToF and AoD measurements at the BS shall henceforth be referred *candidate locations*. The process of finding candidate locations is repeated for all multipath components. The actual user location corresponds to the candidate location identified by the maximum number of multipath components.

Errors in ToF measurements cause the BS to incorrectly estimate the path length to the user. Due to inaccurate AoD measurements the BS incorrectly estimate the users bearing. As a result, a candidate locations estimated by MAP-AT using imprecise ToF and AoD information will not coincide with the users true location. However, it is likely that the candidate locations will be close to the users true location, and hence close to one-another. MAP-AT is modified to first group the candidate locations that are close to one another (at a distance of up to 40 cm) and then estimate the user position to be the centroid of the candidate location group with maximal members.

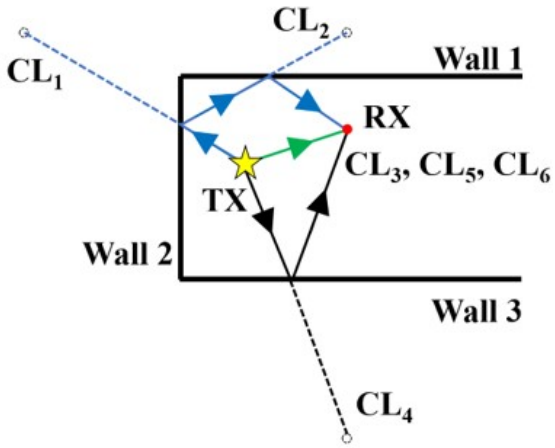

Fig. 20: Three multipath components arrive at the user (RX) shown above - one LOS component (in green) and two NLOS components (in blue and black). Of the six candidate locations for the user (RX), based on AoD and ToF measurements at the BS (TX) ($CL_1 - CL_6$), three candidate locations ($CL_3,\ CL_5,\ CL_6$) correspond to the actual location of the user. The position of the user is estimated to be the modal candidate location (i.e. $CL_3,\ CL_5,\ CL_6$).

If the user is a TX, a similar technique can be used for user localization, using AoA information at the BS and doing backwards ray tracing instead of forwards ray tracing.

1) Simulation Environment: Simulations of localization using candidate locations were done by synthesizing ToF and AoD measurements at 30 BS-user combinations using NYU-Ray, of which 18 were in NLOS and 12 were in LOS. The BS and user locations were taken from previous indoor propagation measurement campaigns conducted in the NYU WIRELESS research center on the 9th floor of 2 MetroTech Center in downtown Brooklyn, New York [169]. The research center has an open-office architecture, with cubicles, walls made of drywalls and windows. The entire floor has dimensions of 35 m by 65.5 m as shown in Fig. 22.

The position of each user was determined using a single BS. To make the simulations realistic, zero mean Gaussian noise with standard deviation σ_{ToF} and σ_{AoD} was added to the ToF and AoD measurements. The positioning error for each RX was defined to be equal to the Euclidean distance between the position estimate and the true position of the RX.

2) Localization Error Analysis: The cumulative distribution function (CDF) for the root mean squared (rms) positioning error in presence of Gaussian noise over 100 simulation runs at each user location is plotted in Fig. 21. When σ_{AoD} = 0.5° and σ_{ToF} = 0.25 ns, the median positioning error was 6.7 cm. Three concentric error circles of radii equal to the rms positioning error corresponding to the three levels of noise added to ToF measurements have been drawn centered at each user location in Fig. 22. The error circles for two outlier user locations having errors of 4.0 m and 4.9 m have not been plotted. The localization error of the outliers can be reduced

This article has been accepted for publication in a future issue of this journal, but has not been fully edited. Content may change prior to final publication. Citation information: DOI 10.1109/ACCESS.2019.2921522, IEEE Access

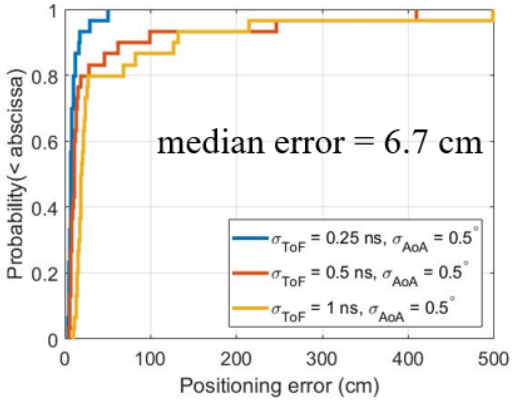

Fig. 21: The CDF of the positioning error, when an RX is localized using a single TX. The median positioning error is 6.7 cm when σ_{ToF} and σ_{AoD} were 0.25 ns and 0.5° respectively.

TABLE VIII: Performance of the map-assisted localization algorithm for different TR separation distances in LOS and NLOS environments at NYU WIRELESS.

TX-RX distance	Env.	Number of User Locations	Mean Localization Error (cm)
<10 m	LOS	6	4.3
	NLOS	11	10.2
10-20 m	LOS	5	8.4
	NLOS	5	10.7
20-30 m	LOS	1	11.4
	NLOS	2	19.0

by using additional BSs for positioning the users [58].

Table VIII illustrates how the localization error varies with TR separation distance in LOS and NLOS environments.

X. Spatial Statistical Channel Modeling

THz frequency poses new challenges for channel modeling. Diffraction effect at THz frequencies will not be as prominent as it is at microwave frequencies. Scattering, instead, is expected to be more notable since the wavelength at THz frequencies are comparable to the size of dust, rain, snow, and roughness of walls [113]. Thus, the THz channel will be even more sparse than the mmWave channels, and LOS and specular reflection may be the only two reliable propagation paths.

A. Spatial Consistency

Spatial consistency, an important channel modeling component, has been acknowledged by 3GPP standards [170]. Most of current statistical channel models are drop-based, which are only able to generate channel impulse responses (CIRs) for a particular user at a randomly picked location in a distance range [171]. There is no spatial correlation between two consecutive simulation runs. Thus, it is impossible to generate dynamic CIRs with spatial correlation based on a users motion within a local area [73], [172], [173]. Spatial consistency enables channel models to provide spatially consistent and smoothly time-evolving CIRs for closely spaced locations.

B. Early Research on Spatial Consistency

Even though spatial consistency is a relatively new channel modeling component, some valuable works have been done not only for channel models but also for channel simulators. 3GPP Release 14 proposed a three-dimensional (3D) geometry-based stochastic channel model (GSCM) and also provided alternative spatial consistency procedures to enable spatially consistent mobility simulations [170]. 5GCM proposed three spatial consistency approaches, which the first one uses spatially correlated random variables as small-scale parameters, and the other two are based on the geometry and fixed locations of scatterers [174]. COST 2100 introduced spatial consistency based on the visible region over which a group of MPCs is visible at a user [175]. QuaDRiGa proposed a time-evolving channel model for user trajectory based on the WINNER II model using geometrical approaches [176]. NYUSIM channel model, a spatial statistical channel model, has also been enabled spatial consistency by generating spatial-correlated large-scale parameters and time-variant small-scale parameters [171]. Some local area measurements in a street canyon scenario have been conducted, and the results indicated that the correlated distance of the large-scale parameters such as the number of time clusters is about 10-15 meters [177].

C. Challenges for Spatial Consistency at mmWave and THz Frequencies

The Doppler shift will be more severe at THz frequencies, which is 90 kHz at 1 THz with a speed of 60 mph. Further, as the channel coherence time decreases, the channel status will change fast and needs to be updated more frequently. Thus, it is critical to provide consecutive and realistic CIRs as time evolves, which can be provided by spatial consistency.

For super resolution imaging, understanding the minor differences of the channel over a few wavelengths, e.g., over hundreds of wavelengths (hundred of micrometers), will require new measurements and models to determine the tiny variations. Statistical modeling for sensing and imaging at THz will require much greater spatial resolution than ever used before in channel modeling.

Most current research on spatial consistency is based on the assumption of omnidirectional antennas at the transmitter and receiver [176], [178]. However, considering that high-gain steerable antennas and beamforming will be used at mmWave and THz frequencies, spatial consistency must be studied and implemented with directionality. When a narrowbeam antenna points to a certain direction, just a few scatterers are illuminated and can generate MPCs. Thus, when the user is moving, the part of environment that can be "seen" will change fast. Spatial consistency needs to be maintained with advanced beam tracking schemes to provide accurate CIRs with time evolution.

Many challenges have not been resolved yet before the actual implementation of spatial consistency for narrowbeam directional antennas. The correlation distances of different parameters are abstracted from field measurements, but most measurements only provide reference correlation distance of spatial consistency for omnidirectional antennas. The antenna beamwidth and the ability of beam steering will have an impact

This article has been accepted for publication in a future issue of this journal, but has not been fully edited. Content may change prior to final publication. Citation information: DOI 10.1109/ACCESS.2019.2921522, IEEE Access

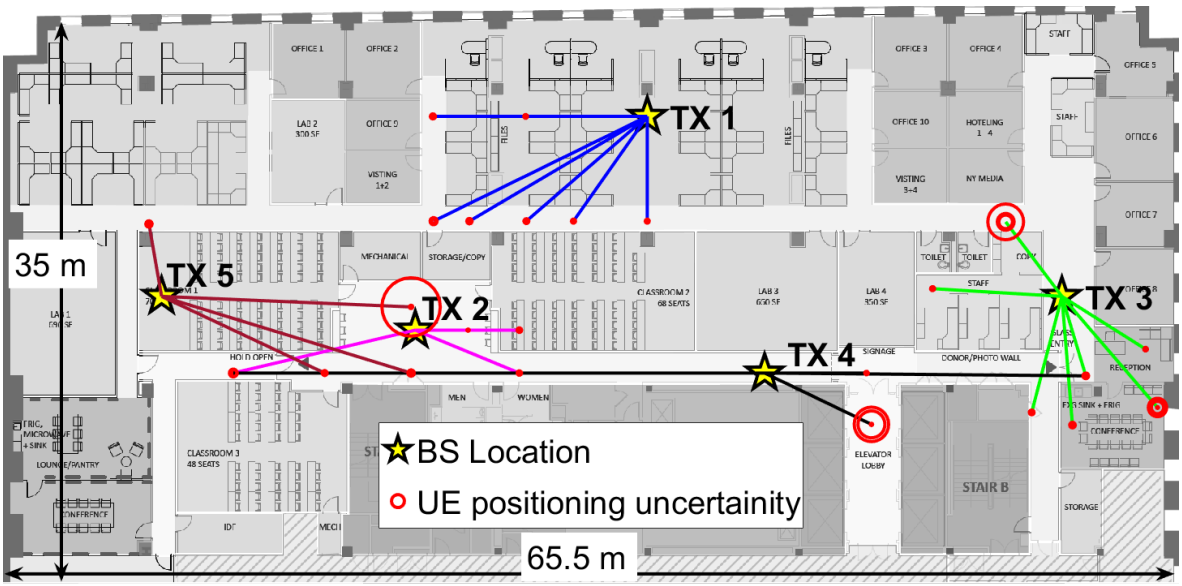

Fig. 22: The three error circles centered at each user location correspond to the rms error over 100 simulations for three noise levels: σ_{ToF} = 0.25, 0.5 and 1 ns with σ_{AoD} = 0.5° in the azimuth and elevation plane. A single BS was used to localize each of the 30 user locations.

on the value of correlation distance, which has not been investigated but will be at much smaller distance scales than ever used before. In addition, more user cases (scenarios) are introduced in the latest 3GPP Release 15 [5] for 5G than the previous generations of cellular systems, and even more user cases will surely evolve into 6G and beyond. Therefore, scenario-specific values of several key channel model parameters will be needed in the future.

XI. Conclusion

This paper has provided a broad and deep look at fundamental opportunities, challenges, and approaches to creating future wireless, sensing, and position location systems for spectrum above 100 GHz, which is likely to be a part of the 6G era in the 2025-2030 time frame. The paper described recent regulatory and standard body activities aimed at fostering future wireless systems that will use multi-GHz bandwidth channels at above 100 GHz, and which may support data rates in excess of 100 Gbps. We demonstrated a large number of promising applications that future THz frequencies will support, as computing power concurrently grows to approach the processing power of the human brain. Many applications of THz wireless will enable novel cognition, sensing, imaging, communications, and positioning capabilities that will be used by automated machinery, autonomous cars, and new human interfaces, all enabled by the ultra-wide bandwidth and ultra-short wavelength at THz which appears to be a promising spectrum for future wireless communications beyond the mmWave regime.

Antenna array technologies will need to exploit new approaches and physical architectures, such as spatial noise-shaping, beamforming, hybrid beamforming, and the *cones of silence*, as these were shown to provide significant performance benefits and will solve design constraints such as the physical size of RF components with a vast number of antenna elements. We also indicated how simultaneous imaging and sensing with location capabilities may be enabled by the move to above 100 GHz. This paper surveyed past work and presented new propagation measurements above 100 GHz, including a comparison of cross-polarization discrimination (XPD) and partition loss measurements for common building materials at 28, 73, and 140 GHz. We also derived scattering theory results that are useful for understanding how the frequency and surface roughness influence scattering behavior across the mmWave and THz bands, and provided reflection/scattering measurements at 140 GHz that validated the Directive Scattering (DS) theory. We noted that extensive measurements in urban, suburban, and rural areas are necessary to study the channel characteristics using statistical and deterministic approaches at frequencies above 100 GHz.

It is clear from this work that THz positioning will support centimeter level accuracy and may also support imaging, even in non line of sight (NLOS) environments. Challenges such as power-efficient devices, cost-effective integrated circuit solutions, and practical phased arrays that may be interconnected with minimal loss loom as impediments to 6G and THz product development, and offer open research and development problems that are being investigated by DARPA and other global research agencies. Other challenges remain, such as how to efficiently construct and code maps of the environment, how to model the THz channel for spatial consistency, and how to reduce computational complexity in spatial multiplexing and beam codebooks for massive numbers of antenna elements, and this paper gave some insights into possible solutions in these areas. Certainly not least, as the world begins to look to 6G and beyond, at frequencies above 100 GHz, there should be careful studies to determine the impact that THz radiation has on the biological effects of humans and animals, and to see if such radiation could be used as a safe and effective replacement for more dangerous ionizing imaging methods such as X-rays and CT/PET scans.

XII. Acknowledgments

This research is supported by the NYU WIRELESS Industrial Affiliates Program and six National Science Foundation (NSF) Research Grants: 1702967, 1731290, 1902283, 1711395, 1854798, and 1730946.

References

[1] B5GS 2018, "The Brooklyn 5G Summit," Apr. 2018. [Online]. Available: https://2018.brooklyn5gsummit.com/

[2] T. S. Rappaport *et al.*, "Millimeter Wave Mobile Communications for 5G Cellular: It Will Work!" *IEEE Access*, vol. 1, pp. 335–349, May 2013.

[3] A.-A. A. Boulogeorgos *et al.*, "Terahertz Technologies to Deliver Optical Network Quality of Experience in Wireless Systems Beyond 5G," *IEEE Communications Magazine*, vol. 56, no. 6, pp. 144–151, June 2018.

[4] T. S. Rappaport, Y. Xing, G. R. MacCartney, A. F. Molisch, E. Mellios, and J. Zhang, "Overview of Millimeter Wave Communications for Fifth-Generation (5G) Wireless Networks-With a Focus on Propagation Models," *IEEE Transactions on Antennas and Propagation*, vol. 65, no. 12, pp. 6213–6230, Dec. 2017.

[5] 3GPP, "Technical Specification Group Radio Access Network; Study on Scenarios and Requirements for Next Generation Access Technologies (Release 15) ," 3rd Generation Partnership Project (3GPP), TR 38.901 V15.0.0, June 2018.

[6] T. S. Rappaport, R. W. Heath, Jr., R. C. Daniels, and J. N. Murdock, *Millimeter Wave Wireless Communications*. Pearson/Prentice Hall, 2015.

[7] T. Kürner and S. Priebe, "Towards THz communications - status in research, standardization and regulation," *Journal of Infrared, Millimeter, and Terahertz Waves*, vol. 35, no. 1, pp. 53–62, Aug 2013.

[8] G. R. MacCartney, Jr. and T. S. Rappaport, "Millimeter-Wave Base Station Diversity for 5G Coordinated Multipoint (CoMP) Applications," *IEEE Transactions on Wireless Communications*, May 2019.

[9] P. H. Siegel, "Terahertz technology," *IEEE Transactions on Microwave Theory and Techniques*, vol. 50, no. 3, pp. 910–928, Mar. 2002.

[10] I. F. Akyildiz, J. M. Jornet, and C. Han, "Terahertz band: Next frontier for wireless communications," *Physical Communication*, vol. 12, pp. 16–32, Sept. 2014.

[11] T. Wu, T. S. Rappaport, and C. M. Collins, "Safe for generations to come: Considerations of safety for millimeter waves in wireless communications," *IEEE Microwave Magazine*, vol. 16, no. 2, pp. 65–84, Mar. 2015.

[12] C. Cho *et al.*, "Characterizing Ionizing Radiation Exposure after T-Cell Depleted Allogeneic Hematopoietic Cell Transplantation," *Biology of Blood and Marrow Transplantation*, vol. 24, issue 3, Supplement, pp. S252–S253, Mar. 2018.

[13] R. Willians, "NASA Space Flight Human System Standard Volume 1: Crew Health," 2012.

[14] National Research Council, *Health risks from exposure to low levels of ionizing radiation: BEIR VII phase 2*. National Academies Press, 2006, vol. 7.

[15] R. Fazel, H. M. Krumholz, Y. Wang, J. S. Ross, J. Chen, H. H. Ting, N. D. Shah, K. Nasir, A. J. Einstein, and B. K. Nallamothu, "Exposure to low-dose ionizing radiation from medical imaging procedures," *New England Journal of Medicine*, vol. 361, no. 9, pp. 849–857, Aug. 2009.

[16] T. Wu, T. S. Rappaport, and C. M. Collins, "The human body and millimeter-wave wireless communication systems: Interactions and implications," in *2015 IEEE International Conference on Communications (ICC)*, June 2015, pp. 2423–2429.

[17] F. 96-326, "Guidelines for evaluating the environmental effects of radio frequency radiation," Aug. 1996.

[18] I. C. on Non-Ionizing Radiation Protection *et al.*, "ICNIRP statement on the guidelines for limiting exposure to time-varying electric, magnetic, and electromagnetic fields (up to 300 GHz)," *Health physics*, vol. 97, no. 3, pp. 257–258, Sept. 2009.

[19] A. Maltsev *et al.*, "Channel models for IEEE 802.11ay," doc.: IEEE 802.11-15/1150r9, Mar. 2017.

[20] "IEEE Standard for High Data Rate Wireless Multi-Media Networks–Amendment 2: 100 Gb/s Wireless Switched Point-to-Point Physical Layer," *IEEE Std 802.15.3d-2017 (Amendment to IEEE Std 802.15.3-2016 as amended by IEEE Std 802.15.3e-2017)*, pp. 1–55, Oct. 2017.

[21] M. J. W. Rodwell, Y. Fang, J. Rode, J. Wu, B. Markman, S. T. uran Brunelli, J. Klamkin, and M. Urteaga, "100-340GHz Systems: Transistors and Applications," in *2018 IEEE International Electron Devices Meeting (IEDM)*, Dec. 2018, pp. 14.3.1–14.3.4.

[22] H. Aggrawal, P. Chen, M. M. Assefzadeh, B. Jamali, and A. Babakhani, "Gone in a picosecond: Techniques for the generation and detection of picosecond pulses and their applications," *IEEE Microwave Magazine*, vol. 17, no. 12, pp. 24–38, Dec. 2016.

[23] D. M. Mittleman, "Twenty years of terahertz imaging," *Opt. Express*, vol. 26, no. 8, pp. 9417–9431, Apr. 2018.

[24] M. Tonouchi, "Cutting-edge terahertz technology," *Nature photonics*, vol. 1, no. 2, pp. 97–105, Feb. 2007.

[25] J. Harvey *et al.*, "Exploiting High Millimeter Wave Bands for Military Communications,Applications, and Design," *IEEE Access*, vol. 7, pp. 52 350 – 52 359, Apr. 2019.

[26] W. Chappel, "Briefing prepared for T-MUSIC Proposer's Day," Jan. 2019.

[27] H. Wang *et al.*, "Power amplifiers performance survey 2000-present," [Online]. Available: https://gems.ece.gatech.edu/PA_survey.html, 2019.

[28] Y. Xing and T. S. Rappaport, "Propagation Measurement System and Approach at 140 GHzMoving to 6G and Above 100 GHz," in *IEEE 2018 Global Communications Conference*, Dec. 2018, pp. 1–6.

[29] R. Piesiewicz, T. Kleine-Ostmann, N. Krumbholz, D. Mittleman, M. Koch, J. Schoebei, and T. Kürner, "Short-range ultra-broadband terahertz communications: Concepts and perspectives," *IEEE Antennas and Propagation Magazine*, vol. 49, no. 6, pp. 24–39, Dec. 2007.

[30] J. Ma, R. Shrestha, J. Adelberg, C.-Y. Yeh, Z. Hossain, E. Knightly, J. M. Jornet, and D. M. Mittleman, "Security and eavesdropping in terahertz wireless links," *Nature*, vol. 563, no. 7729, p. 89, Oct. 2018.

[31] J. N. Murdock and T. S. Rappaport, "Consumption factor: A figure of merit for power consumption and energy efficiency in broadband wireless communications," in *2011 IEEE GLOBECOM Workshops (GC Wkshps)*, Dec. 2011, pp. 1393–1398.

[32] ——, "Consumption factor and power-efficiency factor: A theory for evaluating the energy efficiency of cascaded communication systems," *IEEE Journal on Selected Areas in Communications*, vol. 32, no. 2, pp. 221–236, Feb. 2014.

[33] FCC, "Notice of Proposed Rulemaking: ET Docket No. 18-21," Feb. 2018.

[34] ETSI, "millimeter Wave Transmission (mWT); Applications and use cases of milliimeter wave transmission," Aug. 2015.

[35] M. J. Marcus, "WRC-19 Issues: Agenda Item 1.15 and the Use of 275 - 450 GHz," *IEEE Wireless Communications*, vol. 23, no. 6, pp. 2–3, Dec. 2016.

[36] T. Nagatsuma, "Breakthroughs in photonics 2013: Thz communications based on photonics," *IEEE Photonics Journal*, vol. 6, no. 2, pp. 1–5, Apr. 2014.

[37] X. Yu *et al.*, "400-GHz Wireless Transmission of 60-Gb/s Nyquist-QPSK Signals Using UTC-PD and Heterodyne Mixer," *IEEE Transactions on Terahertz Science and Technology*, vol. 6, no. 6, pp. 765–770, Nov. 2016.

[38] J. Ma, N. J. Karl, S. Bretin, G. Ducournau, and D. M. Mittleman, "Frequency-division multiplexer and demultiplexer for terahertz wireless links," *Nature Comm.*, vol. 8, no. 1, pp. 729–737, Feb. 2017.

[39] S. Mumtaz, J. M. Jornet, J. Aulin, W. H. Gerstacker, X. Dong, and B. Ai, "Terahertz communication for vehicular networks," *IEEE Transactions on Vehicular Technology*, vol. 66, no. 7, pp. 5617–5625, July 2017.

[40] FCC, "Spectrum horizons," *First Report and Order ET Docket 18-21*, Mar. 2019.

[41] mmWave Coalition, "mmWave Coalition's NTIA comments," Jan. 2019. [Online]. Available: http://mmwavecoalition.org/mmwave-coalition-millimeter-waves/mmwave-coalitions-ntia-comments/

[42] V. Petrov, D. Moltchanov, and Y. Koucheryavy, "Applicability assessment of terahertz information showers for next-generation wireless networks," in *2016 IEEE International Conference on Communications (ICC)*, May 2016, pp. 1–7.

[43] V. Petrov, A. Pyattaev, D. Moltchanov, and Y. Koucheryavy, "Terahertz band communications: Applications, research challenges, and standardization activities," in *2016 8th International Congress on Ultra Modern Telecommunications and Control Systems and Workshops (ICUMT)*, Oct. 2016, pp. 183–190.

[44] K. Sengupta, T. Nagatsuma, and D. M. Mittleman, "Terahertz integrated electronic and hybrid electronic–photonic systems," *Nature Electronics*, vol. 1, no. 12, p. 622, Dec. 2018.

[45] S. Chinchali *et al.*, "Network Offloading Policies for Cloud Robotics: a Learning-based Approach," *arXiv preprint arXiv:1902.05703*, Feb. 2019.

[46] S. Garg *et al.*, "Enabling the Next Generation of Mobile Robotics using 5G Wireless," *submitted to Proceedings of IEEE*, .

[47] M. Chen *et al.*, "Cognitive internet of vehicles," *Computer Communications*, vol. 120, pp. 58–70, May 2018.

[48] X.-F. Teng, Y.-T. Zhang, C. C. Poon, and P. Bonato, "Wearable medical systems for p-health," *IEEE reviews in Biomedical engineering*, vol. 1, pp. 62–74, Dec. 2008.

[49] D. M. Mittleman, R. H. Jacobsen, R. Neelamani, R. G. Baraniuk, and M. C. Nuss, "Gas sensing using terahertz time-domain spectroscopy," *Applied Physics B: Lasers and Optics*, vol. 67, no. 3, pp. 379–390, Sept. 1998.

[50] M. Aladsani, A. Alkhateeb, and G. C. Trichopoulos, "Leveraging mmWave Imaging and Communications for Simultaneous Localization and Mapping," in *International Conference on Acoustics, Speech, and Signal Processing (ICASSP)*, May 2019, pp. 1–4.

[51] S. Koenig *et al.*, "Wireless sub-THz communication system with high data rate," *Nature photonics*, vol. 7, no. 12, p. 977, Oct. 2013.

[52] T. S. Rappaport, "6G and Beyond: Terahertz Communications and Sensing," *2019 Brooklyn 5G Summit Keynote*, Apr. 2019. [Online]. Available: https://ieeetv.ieee.org/conference-highlights/ted-tours-brooklyn-5g-summit-2019?

[53] O. Kanhere and T. S. Rappaport, "Position locationing for millimeter wave systems," in *IEEE 2018 Global Communications Conference*, Dec. 2018, pp. 1–6.

[54] R. Kurtzweil, "The age of spiritual machines: When computers exceed human intelligence," *New York, NY: Penguin Books*, 1999.

[55] H. Moravec, "When will computer hardware match the human brain," *Journal of evolution and technology*, vol. 1, no. 1, p. 10, 1998.

[56] *Personal Communications with Paul Horn, former CTO of IBM and Chief Science Officer of New York University*, 2018.

[57] H. Wang and T. S. Rappaport, "A parametric formulation of the UTD diffraction coefficient for real-time propagation prediction modeling," *IEEE Antennas and Wireless Propagation Letters*, vol. 4, pp. 253–257, Aug. 2005.

[58] O. Kanhere, S. Ju, Y. Xing, and T. S. Rappaport, "Map Assisted Millimeter Wave Localization for Accurate Position Location," in *submitted to IEEE Globecom*, Dec. 2019, pp. 1–6.

[59] D. M. Mittleman, "Perspective: Terahertz science and technology," *Journal of Applied Physics*, vol. 122, no. 23, p. 230901, Dec. 2017.

[60] M. J. W. Rodwell, "Sub-mm-wave technologies: Systems, ICs, THz transistors," in *2013 Asia-Pacific Microwave Conference Proceedings (APMC)*, Nov. 2013, pp. 509–511.

[61] S. Kiran Doddalla and G. C. Trichopoulos, "Non-Line of Sight Terahertz imaging from a Single Viewpoint," in *2018 IEEE/MTT-S International Microwave Symposium-IMS*, June 2018, pp. 1527–1529.

[62] S. Ju *et al.*, "Scattering Mechanisms and Modeling for Terahertz Wireless Communications," in *Proc. IEEE International Conference on Communications*, May 2019, pp. 1–7.

[63] A. Velten, T. Willwacher, O. Gupta, A. Veeraraghavan, M. G. Bawendi, and R. Raskar, "Recovering three-dimensional shape around a corner using ultrafast time-of-flight imaging," *Nature communications*, vol. 3, p. 745, Mar. 2012.

[64] M. O. Toole, D. B. Lindell, and G. Wetzstein, "Confocal non-line-of-sight imaging based on the light-cone transform," *Nature*, vol. 555, no. 7696, p. 338, Mar. 2018.

[65] F. Xu, G. Shulkind, C. Thrampoulidis, J. H. Shapiro, A. Torralba, F. N. Wong, and G. W. Wornell, "Revealing hidden scenes by photon-efficient occlusion-based opportunistic active imaging," *Optics express*, vol. 26, no. 8, pp. 9945–9962, Apr. 2018.

[66] A. Sume, M. Gustafsson, M. Herberthson, A. Janis, S. Nilsson, J. Rahm, and A. Orbom, "Radar detection of moving targets behind corners," *IEEE Transactions on Geoscience and Remote Sensing*, vol. 49, no. 6, pp. 2259–2267, June 2011.

[67] K. Thai, O. Rabaste, J. Bosse, D. Poullin, I. Hinostroza, T. Letertre, and T. Chonavel, "Around-the-corner radar: Detection and localization of a target in non-line of sight," in *2017 IEEE Radar Conference (RadarConf)*, May 2017, pp. 0842–0847.

[68] P. Setlur, T. Negishi, N. Devroye, and D. Erricolo, "Multipath exploitation in non-los urban synthetic aperture radar," *IEEE Journal of Selected Topics in Signal Processing*, vol. 8, no. 1, pp. 137–152, Feb. 2014.

[69] R. Zetik, M. Eschrich, S. Jovanoska, and R. S. Thoma, "Looking behind a corner using multipath-exploiting uwb radar," *IEEE Transactions on Aerospace and Electronic Systems*, vol. 51, no. 3, pp. 1916–1926, July 2015.

[70] T. S. Rappaport *et al.*, "Small-scale, local area, and transitional millimeter wave propagation for 5G communications," *IEEE Transactions on Antennas and Propagation*, vol. 65, no. 12, pp. 6474–6490, Dec. 2017.

[71] G. C. Trichopoulos, H. L. Mosbacker, D. Burdette, and K. Sertel, "A Broadband Focal Plane Array Camera for Real-time THz Imaging Applications," *IEEE Transactions on Antennas and Propagation*, vol. 61, no. 4, pp. 1733–1740, Apr. 2013.

[72] T. Chi, M. Huang, S. Li, and H. Wang, " A packaged 90-to-300 GHz transmitter and 115-to-325GHz coherent receiver in CMOS for full-band continuous-wave mm-wave hyperspectral imaging," in *2017 IEEE International Solid-State Circuits Conference (ISSCC)*, Feb 2017, pp. 304–305.

[73] S. Sun *et al.*, "Propagation models and performance evaluation for 5G millimeter-wave bands," *IEEE Transactions on Vehilcular Technology*, July 2018.

[74] S. Sun, T. S. Rappaport, and M. Shafi, "Hybrid beamforming for 5g millimeter-wave multi-cell networks," *IEEE Conference on Computer Communications Workshops (INFOCOM WKSHPS)*, Apr. 2018.

[75] D. J. Allstot, X. Li, and S. Shekhar, "Design considerations for CMOS low-noise amplifiers," in *2004 IEE Radio Frequency Integrated Circuits (RFIC) Systems. Digest of Papers*, June 2004, pp. 97–100.

[76] L. T. Bruton and N. Bartley, "Three-dimensional image processing using the concept of network resonance," *IEEE Transactions on Circuits and Systems*, vol. 32, no. 7, pp. 664–672, July 1985.

[77] L. T. Bruton, "Selective filtering of spatio-temporal plane waves using 3D cone filter banks," in *2001 IEEE Pacific Rim Conference on Communications, Computers and Signal Processing (IEEE Cat. No. 01CH37233)*, vol. 1. IEEE, Aug. 2001, pp. 67–70.

[78] ——, "Three-dimensional cone filter banks," *IEEE Transactions on Circuits and Systems I: Fundamental Theory and Applications*, vol. 50, no. 2, pp. 208–216, Feb. 2003.

[79] N. Liyanage, L. T. Bruton, and P. Agathoklis, "On the attenuation of interference and mutual coupling in antenna arrays using 3D space-time filters," in *2009 IEEE Pacific Rim Conference on Communications, Computers and Signal Processing*. IEEE, Aug. 2009, pp. 146–151.

[80] C. U. Edussooriya, L. T. Bruton, P. Agathoklis, and T. K. Gunaratne, "Low-complexity maximally-decimated multirate 3-D spatio-temporal FIR cone and frustum filters," *IEEE Transactions on Circuits and Systems I: Regular Papers*, vol. 60, no. 7, pp. 1845–1856, Mar. 2013.

[81] S. Handagala, A. Madanayake, L. Belostotski, and L. T. Bruton, "Delta-sigma noise shaping in 2D spacetime for uniform linear aperture array receivers," in *2016 Moratuwa Engineering Research Conference (MERCon)*. IEEE, Apr. 2016, pp. 114–119.

[82] Y. Wang, S. Handagala, A. Madanayake, L. Belostotski, and S. Mandal, "N-port LNAs for mmW array processors using 2-D spatio-temporal $\Delta - \Sigma$ noise-shaping," in *2017 IEEE 60th International Midwest Symposium on Circuits and Systems (MWSCAS)*, Aug. 2017, pp. 1473–1476.

[83] A. Nikoofard, J. Liang, M. Twieg, S. Handagala, A. Madanayake, L. Belostotski, and S. Mandal, "Low-complexity N-port ADCs using 2-D $\Delta - \Sigma$ noise-shaping for N-element array receivers," in *2017 IEEE 60th International Midwest Symposium on Circuits and Systems (MWSCAS)*, Aug. 2017, pp. 301–304.

[84] A. Madanayake, N. Akram, S. Mandal, J. Liang, and L. Belostotski, "Improving ADC figure-of-merit in wideband antenna array receivers using multidimensional space-time delta-sigma multiport circuits," in *2017 10th International Workshop on Multidimensional (nD) Systems (nDS)*, Sept. 2017, pp. 1–6.

[85] Y. Wang, J. Liang, S. Handagala, A. Madanayake, and S. Mandal, " $\Delta - \Sigma$ Noise-Shaping in 2-D Space-Time for Wideband Antenna Array Receivers," *IEEE Transactions on Circuits and Systems I: Regular Papers*, vol. 66, no. 2, pp. 569–582, Sept. 2018.

[86] Y. Wang, J. Liang, L. Belostotski, A. Madanayake, and S. Mandal, "$\Delta - \Sigma$ noise-shaping in 3-D space–time for 2-D wideband antenna array receivers," *Multidimensional Systems and Signal Processing*, pp. 1–23, Oct. 2018.

[87] S. Pavan, R. Schreier, and G. C. Temes, *Understanding Delta-Sigma Data Converters (IEEE Press Series on Microelectronic Systems)*. Wiley-IEEE Press, 2017.

[88] H. Zhao, S. Mandal, V. Ariyarathna, A. Madanayake, and R. J. Cintra, "An Offset-Canceling Approximate-DFT Beamforming Architecture for Wireless Transceivers," in *2018 IEEE International Symposium on Circuits and Systems (ISCAS)*, May 2018, pp. 1–5.

[89] V. Ariyarathna, D. F. G. Coelho, S. Pulipati, R. J. Cintra, F. M. Bayer, V. S. Dimitrov, and A. Madanayake, "Multibeam Digital Array Receiver Using a 16-Point Multiplierless DFT Approximation," *IEEE Transactions on Antennas and Propagation*, vol. 67, no. 2, pp. 925–933, Feb. 2019.

[90] S. Kulasekera, A. Madanayake, D. Suarez, R. J. Cintra, and F. M. Bayer, "Multi-beam receiver apertures using multiplierless 8-point approximate DFT," in *2015 IEEE Radar Conference (RadarCon)*, May 2015, pp. 1244–1249.

[91] D. Suarez, R. J. Cintra, F. M. Bayer, A. Sengupta, S. Kulasekera, and A. Madanayake, "Multi-beam RF aperture using multiplierless FFT approximation," *Electronics Letters*, vol. 50, no. 24, pp. 1788–1790, Dec. 2014.

[92] V. Ariyarathna, S. Kulasekera, A. Madanayake, K. Lee, D. Suarez, R. J. Cintra, F. M. Bayer, and L. Belostotski, "Multi-beam 4 GHz microwave apertures using current-mode DFT approximation on 65 nm CMOS," in *2015 IEEE MTT-S International Microwave Symposium*, May 2015, pp. 1–4.

[93] V. Ariyarathna, A. Madanayake, X. Tang, D. Coelho, R. J. Cintra, L. Belostotski, S. Mandal, and T. S. Rappaport, "Analog Approximate-FFT 8/16-Beam Algorithms, Architectures and CMOS Circuits for 5G Beamforming MIMO Transceivers," *IEEE Journal on Emerging and Selected Topics in Circuits and Systems*, vol. 8, no. 3, pp. 466–479, Sept. 2018.

[94] S. Kulasekera, A. Madanayake, C. Wijenayake, F. M. Bayer, D. Suarez, and R. J. Cintra, "Multi-beam 8×8 RF aperture digital beamformers using multiplierless 2-D FFT approximations," in *2015 Moratuwa Engineering Research Conference (MERCon)*, Apr. 2015, pp. 260–264.

[95] S. M. Perera, V. Ariyarathna, N. Udayanga, A. Madanayake, G. Wu, L. Belostotski, Y. Wang, S. Mandal, R. J. Cintra, and T. S. Rappaport, "Wideband N-Beam Arrays Using Low-Complexity Algorithms and Mixed-Signal Integrated Circuits," *IEEE Journal of Selected Topics in Signal Processing*, vol. 12, May 2018.

[96] A. Madanayake, V. Ariyarathna, N. Udayanga, L. Belostotski, S. K. Perera, and R. J. Cintra, "Design of a low-complexity wideband analog true-time-delay 5-beam array in 65nm CMOS," in *2017 IEEE 60th International Midwest Symposium on Circuits and Systems (MWSCAS)*, Aug. 2017, pp. 1204–1207.

[97] V. Ariyarathna, N. Udayanga, A. Madanayake, S. M. Perera, L. Belostotski, and R. J. Cintra, "Design methodology of an analog 9-beam squint-free wideband IF multi-beamformer for mmW applications," in *2017 Moratuwa Engineering Research Conference (MERCon)*, May 2017, pp. 236–240.

[98] N. Reiskarimian, T. Dinc, J. Zhou, T. Chen, M. B. Dastjerdi, J. Diakonikolas, G. Zussman, and H. Krishnaswamy, "One-Way Ramp to a Two-Way Highway: Integrated Magnetic-Free Nonreciprocal Antenna Interfaces for Full-Duplex Wireless," *IEEE Microwave Magazine*, vol. 20, no. 2, pp. 56–75, Feb. 2019.

[99] N. Reiskarimian and H. Krishnaswamy, "Magnetic-free non-reciprocity based on staggered commutation," *Nature communications*, vol. 7, p. 11217, 2016.

[100] H. J. Liebe, T. Manabe, and G. A. Hufford, "Millimeter-wave attenuation and delay rates due to fog/cloud conditions," *IEEE transactions on antennas and propagation*, vol. 37, no. 12, pp. 1617–1612, Dec. 1989.

[101] T. S. Rappaport, J. N. Murdock, and F. Gutierrez, "State of the art in 60-GHz integrated circuits and systems for wireless communications," *Proceedings of the IEEE*, vol. 99, no. 8, pp. 1390–1436, Aug. 2011.

[102] Y. Yang, M. Mandehgar, and D. Grischkowsky, "Determination of the water vapor continuum absorption by THz-TDS and Molecular Response Theory," *Opt. Express*, vol. 22, no. 4, pp. 4388–4403, Feb. 2014.

[103] J. Ma, J. Adelberg, R. Shrestha, L. Moeller, and D. M. Mittleman, "The Effect of Snow on a Terahertz Wireless Data Link," vol. 39, pp. 505–508, Mar. 2018.

[104] J. Ma, R. Shrestha, L. Moeller, and D. M. Mittleman, "Channel performance for indoor and outdoor terahertz wireless links," *APL Photonics*, vol. 3, no. 5, pp. 1–13, Feb. 2018.

[105] ITU-R, "Attenuation by Atmospheric Gases," Tech. Rep. P.676-11, Sept. 2016.

[106] S. Sun, G. R. MacCartney, Jr., and T. S. Rappaport, "A Novel Millimeter-Wave channel simulator and applications for 5G wireless communications," in *IEEE International Conference on Communication (ICC)*, May 2017, pp. 1–7.

[107] G. R. MacCartney, Jr. and T. S. Rappaport, "Rural macrocell path loss models for millimeter wave wireless communications," *IEEE Journal on Selected Areas in Communications*, vol. 35, no. 7, pp. 1663–1677, July 2017.

[108] H. Xu *et al.*, "Measurements and models for 38-GHz point-to-multipoint radiowave propagation," *IEEE Journal on Selected Areas in Communications*, vol. 18, no. 3, pp. 310–321, Mar. 2000.

[109] ITU-R, "Specific attenuation model for rain for use in prediction methods, propagation in non-ionized media," Tech. Rep. P.838-3, Mar. 2005.

[110] Z. Qingling and J. Li, "Rain attenuation in millimeter wave ranges," in *2006 7th International Symposium on Antennas, Propagation & EM Theory*. IEEE, Oct. 2006, pp. 1–4.

[111] K. Su, L. Moeller, R. B. Barat, and J. F. Federici, "Experimental comparison of performance degradation from terahertz and infrared wireless links in fog," *J. Opt. Soc. Am. A*, vol. 29, no. 2, pp. 179–184, Feb. 2012.

[112] ——, "Experimental comparison of terahertz and infrared data signal attenuation in dust clouds," *J. Opt. Soc. Am. A*, vol. 29, no. 11, pp. 2360–2366, Nov. 2012.

[113] J. Ma, L. Moeller, and J. F. Federici, "Experimental comparison of terahertz and infrared signaling in controlled atmospheric turbulence," *Journal of Infrared, Millimeter, and Terahertz Waves*, vol. 36, no. 2, pp. 130–143, Feb. 2015.

[114] J. Ma, F. Vorrius, L. Lamb, L. Moeller, and J. F. Federici, "Comparison of experimental and theoretical determined terahertz attenuation in controlled rain," *Journal of Infrared, Millimeter, and Terahertz Waves*, vol. 36, no. 12, pp. 1195–1202, Dec. 2015.

[115] E. Moon, T. Jeon, and D. R. Grischkowsky, "Long-Path THz-TDS Atmospheric Measurements Between Buildings," *IEEE Transactions on Terahertz Science and Technology*, vol. 5, no. 5, pp. 742–750, Sept. 2015.

[116] G. R. MacCartney, Jr. *et al.*, "Millimeter-Wave Human Blockage at 73 GHz with a Simple Double Knife-Edge Diffraction Model and Extension for Directional Antennas," in *2016 IEEE 84th Vehicular Technology Conference (VTC2016-Fall)*, Sept. 2016, pp. 1–6.

[117] G. R. MacCartney, Jr., T. S. Rappaport, and S. Rangan, "Rapid fading due to human blockage in pedestrian crowds at 5g millimeter-wave frequencies," in *2017 IEEE Global Communications Conference (GLOBECOM)*, Dec. 2017, pp. 1–7.

[118] T. S. Rappaport, *Wireless Communications: Principles and Practice*, 2nd ed. Upper Saddle River, NJ: Prentice Hall, 2002.

[119] W. L. Chan, J. Deibel, and D. M. Mittleman, "Imaging with terahertz radiation," *Reports on progress in physics*, vol. 70, no. 8, p. 1325, July 2007.

[120] S. Rey, J. M. Eckhardt, B. Peng, K. Guan, and T. Kürner, "Channel sounding techniques for applications in THz communications: A first correlation based channel sounder for ultra-wideband dynamic channel measurements at 300 GHz," in *2017 9th International Congress on Ultra Modern Telecommunications and Control Systems and Workshops (ICUMT)*, Nov. 2017, pp. 449–453.

[121] G. R. MacCartney, Jr. and T. S. Rappaport, "A flexible millimeter-wave channel sounder with absolute timing," *IEEE Journal on Selected Areas in Communications*, vol. 35, no. 6, pp. 1402–1418, June 2017.

[122] G. R. MacCartney, H. Yan, S. Sun, and T. S. Rappaport, "A flexible wideband millimeter-wave channel sounder with local area and NLOS to LOS transition measurements," in *2017 IEEE International Conference on Communications (ICC)*, May 2017, pp. 1–7.

[123] T.Wu, T. S. Rappaport, M. Knox, and D. Shahrjerdi, "A Wideband Sliding Correlator-Based Channel Sounder with Synchronization in 65 nm CMOS," in *IEEE 2019 International Symposium on Circuits and Systems (ISCAS)*, May 2019, pp. 1–5.

[124] S. Bhardwaj, N. K. Nahar, and J. L. Volakis, "All electronic propagation loss measurement and link budget analysis for 350 ghz communication link," *Microwave and Optical Technology Letters*, vol. 59, no. 2, pp. 415–423, July 2016.

[125] S. Priebe, C. Jastrow, M. Jacob, T. Kleine-Ostmann, T. Schrader, and T. Kürner, "Channel and Propagation Measurements at 300 GHz," *IEEE Transactions on Antennas and Propagation*, vol. 59, no. 5, pp. 1688–1698, May 2011.

[126] T. Kleine-Ostmann, C. Jastrow, S. Priebe, M. Jacob, T. Kürner, and T. Schrader, "Measurement of channel and propagation properties at 300 ghz," in *2012 Conference on Precision electromagnetic Measurements*, July 2012, pp. 258–259.

[127] N. Khalid and O. B. Akan, "Wideband THz communication channel measurements for 5G indoor wireless networks," in *2016 IEEE International Conference on Communications (ICC)*, May 2016, pp. 1–6.

[128] I. Sarkas, E. Laskin, J. Hasch, P. Chevalier, and S. P. Voinigescu, "Second generation transceivers for d-band radar and data communication applications," in *2010 IEEE MTT-S International Microwave Symposium*, May 2010, pp. 1328–1331.

[129] S. L. H. Nguyen *et al.*, "Comparing Radio Propagation Channels Between 28 and 140 GHz Bands in a Shopping Mall," *European Conference on Antennas and Propagation*, pp. 1–5, Apr. 2018.

[130] S. L. Nguyen, K. Haneda, and J. Putkonen, "Dual-band multipath cluster analysis of small-cell backhaul channels in an urban street environment," in *Globecom Workshops (GC Wkshps), 2016 IEEE*, Dec. 2016, pp. 1–6.

[131] S. Kim, W. T. Khan, A. Zaji, and J. Papapolymerou, "D-band channel measurements and characterization for indoor applications," *IEEE Transactions on Antennas and Propagation*, vol. 63, no. 7, pp. 3198–3207, July 2015.

[132] C. L. Cheng, S. Kim, and A. Zaji, "Comparison of path loss models for indoor 30 GHz, 140 GHz, and 300 GHz channels," in *2017 11th European Conference on Antennas and Propagation*, Mar. 2017, pp. 716–720.

[133] S. Sun *et al.*, "Investigation of Prediction Accuracy, Sensitivity, and Parameter Stability of Large-Scale Propagation Path Loss Models for 5G Wireless Communications," *IEEE Transactions on Vehicular Technology*, vol. 65, no. 5, pp. 2843–2860, May 2016.

[134] G. R. MacCartney, Jr. *et al.*, "Indoor office wideband millimeter-wave propagation measurements and models at 28 GHz and 73 GHz for ultra-dense 5G wireless networks," *IEEE Access*, pp. 2388–2424, Oct. 2015.

[135] 3GPP, "Study on channel model for frequencies from 0.5 to 100 GHz," TR 38.901 V14.0.0, May 2017.

[136] Bile Peng, S. Rey, and T. Kürner, "Channel characteristics study for future indoor millimeter and submillimeter wireless communications," in *2016 10th European Conference on Antennas and Propagation (EuCAP)*, Apr. 2016, pp. 1–5.

[137] E. R. P. Laura, "Charaterization of sub-THz and mmWave Propagation Channel for Indoor Scenarios," *Eucap*, pp. 1–4, July 2018.

[138] J. M. Jornet and I. F. Akyildiz, "Channel Modeling and Capacity Analysis for Electromagnetic Wireless Nanonetworks in the Terahertz Band," *IEEE Transactions on Wireless Communications*, vol. 10, no. 10, pp. 3211–3221, Oct. 2011.

[139] Y. Xing *et al.*, "Verification and calibration of antenna cross-polarization discrimination and penetration loss for millimeter wave communications," in *2018 IEEE 88th Vehicular Technology Conference*, Aug. 2018, pp. 1–6.

[140] G. R. MacCartney, Jr. and T. S. Rappaport, "73 GHz millimeter wave propagation measurements for outdoor urban mobile and backhaul communications in New York City," in *2014 IEEE International Conference on Communications (ICC)*, June 2014, pp. 4862–4867.

[141] H. T. Friis, "A note on a simple transmission formula," *Proceedings of the IRE*, vol. 34, no. 5, pp. 254–256, May 1946.

[142] R. G. Vaughan, "Polarization diversity in mobile communications," *IEEE Transactions on Vehicular Technology*, vol. 39, no. 3, pp. 177–186, Aug. 1990.

[143] A. Ghosh *et al.*, "Millimeter-Wave Enhanced Local Area Systems: A High-Data-Rate Approach for Future Wireless Networks," *IEEE Journal on Selected Areas in Communications*, vol. 32, no. 6, pp. 1152–1163, June 2014.

[144] T. S. Rappaport and S. Deng, "73 GHz wideband millimeter-wave foliage and ground reflection measurements and models," in *IEEE International Conference on Communications Workshops (ICCW)*, June 2015, pp. 1238–1243.

[145] H. Zhao *et al.*, "28 GHz millimeter wave cellular communication measurements or reflection and penetration loss in and around buildings in New York city," in *2013 IEEE International Conference on Communications (ICC)*, June 2013, pp. 5163–5167.

[146] G. D. Durgin, T. S. Rappaport, and H. Xu, "Measurements and models for radio path loss and penetration loss in and around homes and trees at 5.85 GHz," *IEEE Transactions on Communications*, vol. 46, no. 11, pp. 1484–1496, Nov. 1998.

[147] C. R. Anderson and T. S. Rappaport, "In-building wideband partition loss measurements at 2.5 and 60 GHz," *IEEE Transactions on Wireless Communications*, vol. 3, no. 3, pp. 922–928, May 2004.

[148] J. Ryan, G. R. MacCartney, Jr., and T. S. Rappaport, "Indoor Office Wideband Penetration Loss Measurements at 73 GHz," in *IEEE International Conference on Communications Workshop*, May 2017, pp. 1–6.

[149] J. Kokkoniemi, J. Lehtomki, and M. Juntti, "Measurements on penetration loss in terahertz band," in *2016 10th European Conference on Antennas and Propagation (EuCAP)*, Apr. 2016, pp. 1–5.

[150] Y. P. Zhang and Y. Hwang, "Measurements of the characteristics of indoor penetration loss," in *1994 IEEE 44th Vehicular Technology Conference (VTC)*, vol. 3, June 1994, pp. 1741–1744.

[151] L. M. Frazier, "Radar surveillance through solid materials," in *Command, Control, Communications, and Intelligence Systems for Law Enforcement*, vol. 2938. International Society for Optics and Photonics, Feb. 1997, pp. 139–147.

[152] A. K. M. Isa, A. Nix, and G. Hilton, "Impact of diffraction and attenuation for material characterisation in millimetre wave bands," in *2015 Loughborough Antennas and Propagation Conference (LAPC)*, Nov. 2015, pp. 1–4.

[153] B. Kapilevich, M. Einat, A. Yahalom, M. Kanter, B. Litvak, and A. Gover, "Millimeter Waves Sensing Behind Walls-Feasibility Study With FEL Radiation," *Proceedings of FEL 2007, Novosibirsk, Russia*, 2007.

[154] R. R. Skidmore, T. S. Rappaport, and A. L. Abbott, "Interactive coverage region and system design simulation for wireless communication systems in multifloored indoor environments: SMT PLUS," in *Proceedings of the 5th IEEE International Conference on Universal Personal Communications*, vol. 2, Sept. 1996, pp. 646–650.

[155] S. Y. Seidel and T. S. Rappaport, "900 MHz path loss measurements and prediction techniques for in-building communication system design," in *1991 Proceedings of the 41st IEEE Vehicular Technology Conference*, May 1991, pp. 613–618.

[156] A. A. Goulianos, A. L. Freire, T. Barratt, E. Mellios, P. Cain, M. Rumney, A. Nix, and M. Beach, "Measurements and characterisation of surface scattering at 60 ghz," in *2017 IEEE 86th Vehicular Technology Conference (VTC-Fall)*, Sept. 2017, pp. 1–5.

[157] A. Navarro, D. Guevara, and D. A. Parada, "Diffuse Scattering Implementation and Verification in Ray Launching Based Tool at 5.4 GHz," *32nd URSI GASS, Montreal*, Aug. 2017.

[158] V. Degli-Esposti, F. Fuschini, E. M. Vitucci, and G. Falciasecca, "Measurement and modelling of scattering from buildings," *IEEE Transactions on Antennas and Propagation*, vol. 55, no. 1, pp. 143–153, Jan. 2007.

[159] J. Järveläinen, K. Haneda, M. Kyrö, V. Kolmonen, J. Takada, and H. Hagiwara, "60 GHz radio wave propagation prediction in a hospital environment using an accurate room structural model," in *2012 Loughborough Antennas Propagation Conference (LAPC)*, Nov. 2012, pp. 1–4.

[160] V. Degli-Esposti, "A diffuse scattering model for urban propagation prediction," *IEEE Transactions on Antennas and Propagation*, vol. 49, no. 7, pp. 1111–1113, July 2001.

[161] GPS.gov, "GPS Accuracy," May 2019. [Online]. Available: http://www.gps.gov/systems/gps/performance/accuracy/

[162] J. S. Parke, P. Mickelson, J. Yeak, K. Kremeyer, and J. Rife, "Exploiting the Terahertz Band for Radionavigation," *Journal of Infrared, Millimeter, and Terahertz Waves*, vol. 37, no. 10, pp. 1021–1042, Oct. 2016.

[163] C. D. McGillem and T. S. Rappaport, "A beacon navigation method for autonomous vehicles," *IEEE Transactions on Vehicular Technology*, vol. 38, no. 3, pp. 132–139, Aug. 1989.

[164] B. Peng, K. Guan, and T. Kürner, "Cooperative Dynamic Angle of Arrival Estimation Considering SpaceTime Correlations for Terahertz Communications," *IEEE Transactions on Wireless Communications*, vol. 17, no. 9, pp. 6029–6041, Sept. 2018.

[165] S. U. Pillai, *Array signal processing*. Springer Science & Business Media, 2012.

[166] T. E. Tuncer and B. Friedlander, *Classical and modern direction-of-arrival estimation*. Academic Press, 2009.

[167] P. Meissner, E. Leitinger, M. Fröhle, and K. Witrisal, "Accurate and Robust Indoor Localization Systems Using Ultra-wideband Signals," in *European Navigation Conference (ENC)*, Apr. 2013, pp. 1–9.

[168] A. O. Kaya, L. Greenstein, D. Chizhik, R. Valenzuela, and N. Moayeri, "Emitter Localization and Visualization (ELVIS): A Backward Ray Tracing Algorithm for Locating Emitters," in *2007 41st Annual Conference on Information Sciences and Systems*, Mar. 2007, pp. 376–381.

[169] G. R. MacCartney, Jr., S. Deng, and T. S. Rappaport, "Indoor Office Plan Environment and Layout-Based mmWave Path Loss Models for 28 GHz and 73 GHz," in *2016 IEEE 83rd Vehicular Technology Conference (VTC Spring)*, May 2016, pp. 1–6.

[170] 3GPP, "Technical Specification Group Radio Access Network; Study on channel model for frequencies from 0.5 to 100 GHz (Release 14)," TR 38.901 V14.2.0, Sept. 2017. [Online]. Available: http://www.3gpp.org/DynaReport/38901.htm

[171] S. Ju and T. S. Rappaport, "Simulating motion - incorporating spatial consistency into the nyusim channel model," in *IEEE 88th Vehicular Technology Conference Workshops (VTC2018-Fall WKSHPS)*, Aug. 2018, pp. 1–6.

[172] S. Sun *et al.*, "Millimeter wave small-scale spatial statistics in an urban microcell scenario," in *2017 IEEE International Conference on Communications (ICC)*, May 2017, pp. 1–7.

[173] M. K. Samimi and T. S. Rappaport, "3-D millimeter-wave statistical channel model for 5G wireless system design," *IEEE Transactions on*

Microwave Theory and Techniques, vol. 64, no. 7, pp. 2207–2225, July 2016.

[174] Aalto University, AT&T, BUPT, CMCC, Ericsson, Huawei, Intel, KT Corporation, Nokia, NTT DOCOMO, New York University, Qualcomm, Samsung, University of Bristol, and University of Southern California, "5G Channel Model for bands up to 100 GHz," Tech. Rep., Oct. 2016. [Online]. Available: http://www.5gworkshops.com/5GCM.html

[175] L. Liu, C. Oestges, J. Poutanen, K. Haneda, P. Vainikainen, F. Quitin, F. Tufvesson, and P. D. Doncker, "The COST 2100 MIMO channel model," *IEEE Wireless Communications*, vol. 19, no. 6, pp. 92–99, Dec. 2012.

[176] S. Jaeckel, L. Raschkowski, K. Börner, and L. Thiele, "Quadriga: A 3-d multi-cell channel model with time evolution for enabling virtual field trials," *IEEE Transactions on Antennas and Propagation*, vol. 62, no. 6, pp. 3242–3256, June 2014.

[177] S. Ju and T. S. Rappaport, "Millimeter-wave extended nyusim channel model for spatial consistency," in *2017 IEEE Global Communications Conference (GLOBECOM)*, Dec. 2018, pp. 1–6.

[178] F. Ademaj, M. K. Mueller, S. Schwarz, and M. Rupp, "Modeling of spatially correlated geometry-based stochastic channels," in *2017 IEEE 86th Vehicular Technology Conference (VTC-Fall)*, Sept. 2017, pp. 1–6.

Theodore S. Rappaport (S'83-M'84-SM'91-F'98) is the David Lee/Ernst Weber Professor at New York University (NYU) and holds faculty appointments in the Electrical and Computer Engineering department of the NYU Tandon School of Engineering, the Courant Computer Science department, and the NYU Langone School of Medicine. He is the founder and director of NYU WIRELESS, a multidisciplinary research center focused on the future of wireless communications and applications. His research has led the way for modern wireless communication systems. In 1987, his Ph.D. at Purdue University provided fundamental knowledge of indoor wireless channels used to create the first Wi-Fi standard (IEEE 802.11), and he conducted fundamental work that led to the first US Digital cellphone standards, TDMA IS-54/IS-136 and CDMA IS-95. He and his students engineered the worlds first public wi-fi hotspots, and more recently, his work proved the viability of millimeter waves for mobile communications and the global wireless industry adopted his vision for 5th generation (5G) cellphone networks. He founded three academic wireless research centers at Virginia Tech, University of Texas, and NYU that have produced thousands of engineers and educators since 1990, and he has coauthored over 300 papers and twenty books, including the most cited books on wireless communications, adaptive antennas, wireless simulation, and millimeter-wave communications. He co-founded two wireless companies, TSR Technologies and Wireless Valley Communication, which were sold to publicly traded companies, and he has advised many others. He co-founded the Virginia Tech Symposium on Wireless Communications in 1991, the Texas Wireless Summit in 2003, and the Brooklyn 5G Summit (B5GS) in 2014. He has more than 100 patents, serves on the Technological Advisory Council of the Federal Communications Commission (FCC), is Fellow of the IEEE, Fellow of the Radio Club of America, Fellow of the National Academy of Inventors, a life member of the American Radio Relay League, a licensed professional engineer in Texas and Virginia, and an amateur radio operator (N9NB). He has received ASEEs Terman award, The Sir Monty Finniston Medal from the Institution of Engineering and Technology (IET), the IEEE Vehicular Technology Societys James R. Evans Avant Garde and Stu Meyer awards, the IEEE Education Society William E. Sayle award for achievement in education, the IEEE Communications Society Armstrong award, and the Armstrong Medal from the Radio Club of America.

Yunchou Xing received the B.S. degree in electronic science and technology from Tianjin University, Tianjin, China, in 2014, and the M.S. degree in electrical engineering from the Tandon School of Engineering, New York University (NYU), Brooklyn, NY, USA, in 2016. Now, he is a Ph.D. student with a topic on fifth-generation (5G) millimeter-wave (mmWave) wireless communications under the supervision of Prof. Theodore. S. Rappaport.

He has authored or co-authored 7 technical papers in the field of mmWave wireless communications, including a 2018 IEEE VTC best student paper award for the paper Verification and Calibration of Antenna Cross Polarization Discrimination and Penetration Loss for Millimeter Wave Indoor Communications. His research interests include radio propagation, channel sounding, and channel modeling for ultra-wideband communications systems with a focus on frequencies above 100 GHz.

Ojas Kanhere received the B.Tech. and M.Tech. degrees in electrical engineering from IIT Bombay, Mumbai, India, in 2017. He is currently pursuing the Ph.D. degree in electrical engineering with the NYU WIRELESS Research Center, New York University (NYU) Tandon School of Engineering, Brooklyn, NY, USA, under the supervision of Prof. Rappaport. His research interests include mmWave localization and channel modeling.

Shihao Ju received the B.S. degree in communications engineering from Harbin Institute of Technology, Harbin, China, in 2017 and the M.S. degree in electrical engineering from New York University (NYU), Brooklyn, NY, USA, in 2019. He is currently pursuing the Ph.D. degree in electrical engineering with NYU, Brooklyn, NY, USA, under the supervision of Prof. Theodore S. Rappaport.

He joined NYU WIRELESS Research Center in August 2017. He has three first-author conference publications and co-authored one publication. His current research interest is millimeter-wave and Terahertz channel measurements, channel modeling, and channel simulation.

Dr. Arjuna Madanayake (S'03, M'08) is a tenured Associate Professor at the Department of Electricaland Computer Engineering, Florida International University (FIU) in Miami, Florida, since August 2018. He was a tenured Associate Professor at the Department of Electrical and Computer Engineering, University of Akron, between August 2015- August 2018, anda tenure-track Assistant Professor, at the same department, between December 2009- August 2015. Dr. Madanayake completed his Ph.D. and M.Sc. degrees, both in Electrical Engineering, from the University of Calgary, Canada, and the B.Sc. Engineering in Electronicand Telecommunication Engineering (First Class Honors) from the University of Moratuwa, Sri Lanka, in 2002. He is a past pupil of Ananda Vidyalaya, Colombo 10, Sri Lanka. Dr. Madanayakes research interests span wireless communications, electronics, circuitsand systems, one- and multi-dimensional signal processing, circuit theory and applications, FPGA and digital VLSI, analog IC design, microwave, mm-wave, and sub-THz RF circuits and antenna array processing. His research has recently been supported by severalgrants from DARPA, ONR and NSF.

This article has been accepted for publication in a future issue of this journal, but has not been fully edited. Content may change prior to final publication. Citation information: DOI 10.1109/ACCESS.2019.2921522, IEEE Access

Soumyajit Mandal (S'01, M'09, SM'14) received the B.Tech. degree in electronics and electrical communications engineering from the Indian Institute of Technology, Kharagpur, India, in 2002, and the M.S. and Ph.D. degrees in electrical engineering from the Massachusetts Institute of Technology (MIT), Cambridge, in 2004 and 2009, respectively. He was a research scientist at Schlumberger-Doll Research, Cambridge, MA, from 2010-2014. He is currently the T. and A. Schroeder Assistant Professor in the Department of Electrical Engineering and Computer Science, Case Western Reserve University, Cleveland, OH.

Dr. Mandal's research interests include analog and biological computation, magnetic resonance sensors, low-power analog and RF circuits, and precision instrumentation for various biomedical and sensor interface applications. He received the President of India Gold Medal (2002), the annual MIT Microsystems Technology Laboratories (MTL) Doctoral Dissertation Seminar (2009), the T. Keith Glennan Fellowship (2016), and the IIT Kharagpur Young Alumni Achiever Award (2018). He has over 120 publications in peer-reviewed journals and premier conferences. He is a senior member of the IEEE.

Ahmed Alkhateeb received his B.S. degree (distinction with honor) and M.S. degree in Electrical Engineering from Cairo University, Egypt, in 2008 and 2012, and his Ph.D. degree in Electrical Engineering from The University of Texas at Austin, USA, in August 2016. Between Sept. 2016 and Dec. 2017, he was a Wireless Communications Researcher at the Connectivity Lab, Facebook, in Menlo Park, CA. He joined Arizona State University (ASU) in spring 2018, where he is currently an Assistant Professor in the School of Electrical, Computer and Energy Engineering. He has held R&D internships at FutureWei Technologies (Huawei) in Chicago, IL, and Samsung Research America (SRA) in Dallas, TX. His research interests are in the broad areas of wireless communications, communication theory, signal processing, machine learning, and applied math. Dr. Alkhateeb is the recipient of the 2012 MCD Fellowship from The University of Texas at Austin and the 2016 IEEE Signal Processing Society Young Author Best Paper Award for his work on hybrid precoding and channel estimation in millimeter wave communication systems.

Georgios C. Trichopoulos (M'05) received the Diploma degree in electrical and computer engineering from the Democritus University of Thrace, Xanthi, Greece, in 2004, the M.S. degree in biomedical engineering from the National Technical University of Athens, Athens and University of Patras, Patras, Greece (under a joint program), in 2006, and the Ph.D. degree in electrical and computer engineering from the Ohio State University, Columbus, OH, USA, in 2013. His doctoral work provided fundamental knowledge for the design of real-time terahertz cameras and non-contact probing of mmWave/THz circuits and devices. From 2013-2015, he worked as a Post-doctoral Researcher at the ElectroScience Laboratory, Ohio State University. In 2015, he joined Arizona State University as an Assistant Professor with the School of Electrical, Computer, and Energy Engineering. His research interests are in antennas, microwaves and electromagnetic theory. He focuses on mmWave/THz imaging methods and systems, antenna design for mmWave/THz sensors, and high-frequency device and circuit characterization methods. He received the Best Student Paper Award in the 2013 IEEE Antennas and Propagation Symposium, Orlando, FL and the NSF CAREER Award in 2019.